



Experimental and numerical investigation of the deep rolling process focussing on 34CrNiMo6 railway axles

Tobias Pertoll¹ · Christian Buzzi¹ · Andreas Dutzler^{1,2} · Martin Leitner¹ · Benjamin Seisenbacher³ · Gerhard Winter³ · László Boronkai²

Received: 17 March 2023 / Accepted: 1 July 2023 / Published online: 24 July 2023
© The Author(s) 2023

Abstract

Deep rolling is a powerful tool to increase the service life or reduce the weight of railway axles. Three fatigue-resistant increasing effects are achieved in one treatment: lower surface roughness, strain hardening and compressive residual stresses near the surface. In this work, all measurable changes introduced by the deep rolling process are investigated. A partly deep-rolled railway axle made of high strength steel material 34CrNiMo6 is investigated experimentally. Microstructure analyses, hardness-, roughness-, FWHM- and residual stress measurements are performed. By the microstructure analyses a very local grain distortion, in the range $< 5 \mu\text{m}$, is proven in the deep rolled section. Stable hardness values, but increased strain hardening is detected by means of FWHM and the surface roughness is significantly reduced by the process application. Residual stresses were measured using the XRD and HD methods. Similar surface values are proven, but the determined depth profiles deviate. Residual stress measurements have generally limitations when measuring in depth, but especially their distribution is significant for increasing the durability of steel materials. Therefore, a numerical deep rolling simulation model is additionally built. Based on uniaxial tensile and cyclic test results, examined on specimen machined from the edge layer of the railway axle, an elastic–plastic Chaboche material model is parameterised. The material model is added to the simulation model and so the introduced residual stresses can be simulated. The comparison of the simulated residual stress in-depth profile, considering the electrochemical removal, shows good agreement to the measurement results. The so validated simulation model is able to determine the prevailing residual stress state near the surface after deep rolling the railway axle. Maximum compressive residual stresses up to about $-1,000 \text{ MPa}$ near the surface are achieved. The change from the induced compressive to the compensating tensile residual stress range occurs at a depth of 3.5 mm and maximum tensile residual stresses of $+100 \text{ MPa}$ at a depth of 4 mm are introduced. In summary, the presented experimental and numerical results demonstrate the modifications induced by the deep rolling process application on a railway axle and lay the foundation for a further optimisation of the deep rolling process.

Keywords Mechanical surface treatment · Deep rolling · Railway axle · 34CrNiMo6 · Residual stress · Finite element method

Introduction

The manufacturing process of railway axles can lead to residual stresses in the component, whereas they are often unevenly distributed in the circumference of the railway axle. Both positive tensile and compressive residual stresses can occur. These have a significant influence on the component lifetime, crack initiation and crack propagation [1–3]. A defined residual stress condition in the near-surface area can be accomplished by post-treatments. A well-suited and often used process is the mechanical treatment deep rolling. The process is very popular due to its easy integration

✉ Tobias Pertoll
tobias.pertoll@tugraz.at

¹ Institute of Structural Durability and Railway Technology, Graz University of Technology, Inffeldgasse 25/D, 8010 Graz, Austria

² Siemens Mobility Austria GmbH, Eggenberger Strasse 31, 8020 Graz, Austria

³ Montanuniversität Leoben, Chair of Mechanical Engineering, Franz-Josef-Strasse 18, 8700 Leoben, Austria

into the manufacturing process, its cost-effective application and the effective treatment depth achieved, compared to shot peening and others [4–7].

The process is used in many different industries in addition to railway applications, like in the automotive industry, aerospace, power generation and also medical applications [7–10]. While in other fields some research results have been published, but even in limited quantities, there are still few research results investigating the deep rolling process applied on railway axles [11–15].

During the process application, a deep rolling tool is pressed onto the rotating surface of the component and moved in the feed direction. In the contact area, the material plasticises in the area near to the surface. This achieves three main benefits in one process application. Surface roughness is reduced, the near-surface area is strain hardened and defined compressive residual stresses are introduced. Figure 1 shows a typical residual stress in-depth profile after deep rolling. Near the surface, the maximum residual compressive stresses occur. Below this point, the residual compressive stresses reduce until they change to the compensating range of tensile residual stress with the zero crossing [7].

Depending on the material, the different mechanisms have a fatigue life-increasing effect. Although lower surface roughness has a positive effect on all materials, the significance of work hardening and residual stresses is yield strength and material dependent. Work hardening is more significant for materials with low yield strength, but also for high strength titanium alloys. For materials with a high yield strength, like the investigated steel 34CrNiMo6, the compressive residual stresses have a higher positive impact on the fatigue behaviour [6, 8, 16]. The application of the process has been investigated in several publications. However, due to the strong material dependency, a differentiation to

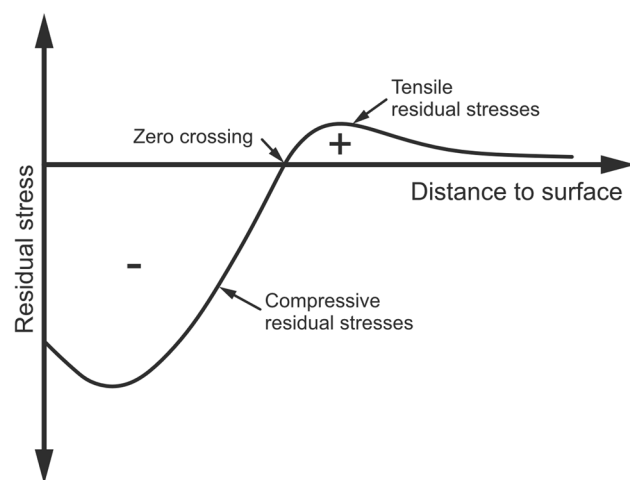


Fig. 1 Typical residual stress in depth profile after deep rolling

the investigated material must be made. There are investigations for titanium alloys [10, 17], aluminium alloys [18, 19] and different steel types, including stainless steels [20–22]. The data available for high-strength steels are in general very limited [23, 24].

The process is mainly applied to rotationally symmetrical components, although applications to flat surfaces and also to welds are considered and investigated in the literature [19, 25, 26]. In addition, attempts are made to combine the process with other post-treatment processes [27–30] and applications at different temperatures [21, 31–33].

In the design standards for cyclically loaded components, such as the DIN 743 [34] or FKM guideline [35], the consideration of post-treatment processes is only considered to a very limited extent and is only permissible for small diameters due to the limited available data. This means for railway axles that the service life-increasing and subsequently also weight-reducing effect of the deep rolling process application can basically not be exploited.

Modern design approaches, based on works such as [36], go one step further and allow the consideration of post-treatment processes. For its application, a detailed knowledge of the hardness and residual stress depth profile is necessary. Although the hardness-depth distribution can be measured, the residual stress depth curve is comparably difficult to establish. Especially the knowledge of the prevailing residual stresses at the surface, the depth of the zero crossing and the depth and amount of the tensile residual stresses is important. These have an influence on the local fatigue behaviour and location where a fatigue crack starts to grow [37]. Near the surface, residual stresses can be determined with both common measurement methods, hole-drilling (HD) and X-ray diffraction (XRD) method. However, the zero-crossing cannot be determined by the two measurement methods accurately. With the HD method, the maximum measurement depth is not sufficient. To determine a depth profile using XRD, the material must be electrochemically removed between the measurement steps. This removes the material with compressive residual stress and thus also reduces the compensating tensile residual stresses beneath. This means that the zero crossing and also the tensile residual stress area cannot be measured using XRD method [1, 10, 38, 39].

The prevailing residual stresses can be determined with the help of a digital model of the process. Different approaches to simulate the happening during and after the deep rolling process application can be found in the literature. Analytical approaches [40–42], classical FE methods [43–46] and accelerated FE methods are published [47, 48]. The highest quality of results can be expected from simulation using the classical FE method, but also the greatest computational effort and calculation time. The simplified representation of the process in a 2D simulation does not

provide satisfactory results [49, 50], the simulation in 3D is more promising.

However, within the framework of the presented research work, a 3D simulation model of the deep rolling process is built as realistically as possible. Specimens are machined from the railway axle and uniaxial tensile and cyclic tests are conducted. Based on the results, an elastic plastic Chaboche material model [51–53] is parameterised for the investigated material 34CrNiMo6 and applied to the simulation model. The difficulty is the appearance of multiple non-linearities. The simulation is validated with measurement data considering the electrochemical removal and thus the possibility is created to determine the residual stress state occurring in the component after the deep rolling process application.

To round up the effect of the deep rolling process on the railway axle, all detectable changes listed in [9] are investigated. In addition to the residual stress and hardness measurements already mentioned, the influence on the microstructure, roughness and work hardening, by means of FWHM values, are investigated and the results are presented.

Therefore, the scientific contribution can be stated as follows:

- Comprehensive experimental investigation of modification of local properties accused by the deep rolling process application
- Detailed investigation and comparison of the most common residual stress measurement techniques
- Presentation of a comprehensively validated numerical simulation model of the deep rolling process
- Numerical consideration of the electrochemical removal in the simulation to ensure comparability to measurement results by XRD technique
- Reliable numerical assessment of the in-depth residual stress profile with special focus on the highest occurring compressive and tensile residual stress values and the depth of zero crossing

Material and specimen design

In [9] the state of knowledge of the deep rolling process is summarised and all measurable parameters and material properties that change as a result of the application of the

process are listed. In the present study, these parameters are collected and investigated on a present partly deep-rolled railway axle. Figure 2 shows the schematic structure of the axle. In addition to two wheel and two bearing seats, one gear and one brake seat are provided. The deep rolled surface regions are marked in red, and the not-treated regions are marked in blue. In addition, the measurement points (MP) 1–4 are marked, where the residual stress measurements are carried out and to which a reference is made in the following sections of the document.

In the following sections, details regarding the applied deep rolling process, the material composition, specimen manufacturing and the performed investigations are presented.

Deep rolling process

The transitions to the seats, which are heavily loaded during operation, are designed by basket arches and are deep rolled, as shown in Fig. 2. The seats and the central cylindrical part remain untreated. The following deep rolling tools and deep rolling parameters are used:

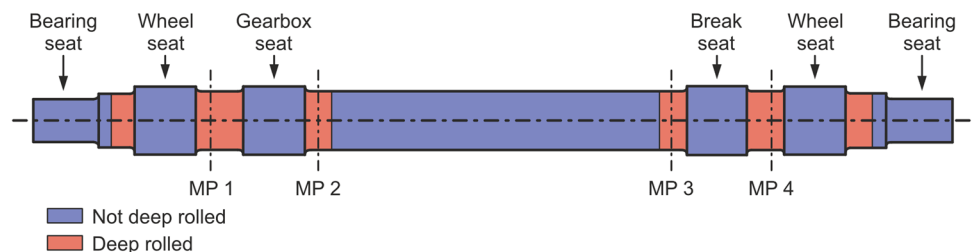
• Deep rolling tool	ECOROLL FAK90 [54]
• Tool geometry	Disc tool
• Tool dimensions	Diameter $D_{Tool} = 100$ mm Contact radius $R_{Contact} = 9$ mm
• Tool arrangement	Twin disc tool
• Deep rolling force	$F = 20$ kN
• Deep rolling feed	0.5 mm/rev

Figure 3 schematically shows the deep rolling procedure applied to the railway axle. The specified deep rolling parameters, the tool properties and arrangement are shown.

Base material

The investigated railway axle base material is a high-strength steel 34CrNiMo6. This material is, in addition to the standardised European steels for railway axles EA1N and EA4T [55], an additionally used steel for high-speed and locomotive applications [4, 54, 56–58].

Fig. 2 Schematic structure of the railway axle with marked deep rolled surface regions (red)



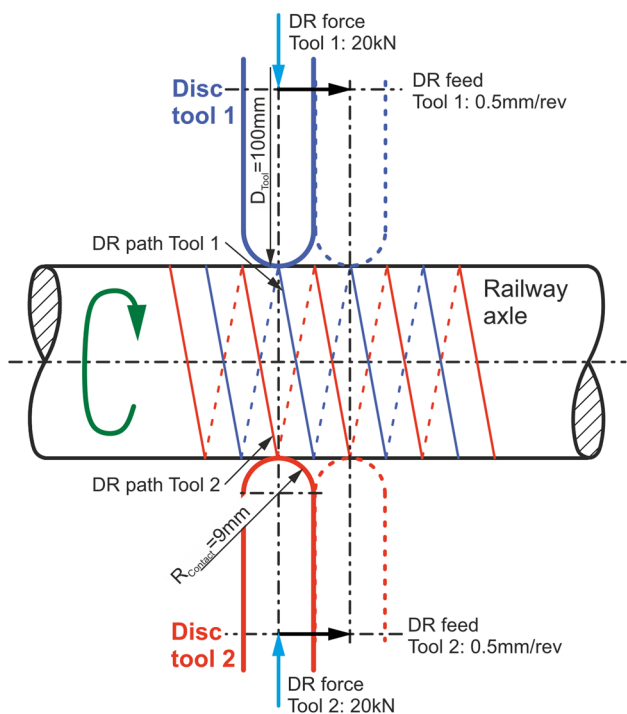


Fig. 3 Schematic illustration of the deep rolling process with tool arrangement

In Table 1 the nominal chemical composition of the melt material is listed in weight percentage. The material of the investigated railway axle meets the required chemical composition [59].

Table 1 Nominal chemical composition of the investigated railway axle made of 34CrNiMo6 in weight % [59]

	C	Si	Mn	P	S	Cr	Mo	Ni	Cu	Other
Nominal (Melt)	0.30 – 0.38	0.10 – 0.40	0.50 – 0.80	0.025	0.035	1.30 – 1.70	0.15 – 0.30	1.30 – 1.70	0.40	-

Sampling

To execute the tensile tests, cyclic tests, hardness in-depth measurements and microstructure analysis, the test specimens must be machined from the railway axle. As shown in Fig. 2, certain surface regions of the examined railway axle are deep rolled and others are not treated. According to this surface condition, areas for sampling of the test specimen are defined. The selected specimen locations at the railway axle are presented in Fig. 4. To prove the properties before the process execution, the specimens for the tensile and low cycle fatigue (LCF) tests were taken from a not deep rolled area. Thus, the initial material properties relevant for the simulation of the deep rolling process are tested in the near-surface area. For the hardness measurements and microstructure analysis, samples from both surface conditions are cut out.

The railway axle is roughly machined using a band saw with the lowest possible heat input. Two disks and two blocks are machined out. From the disks, the test specimen for hardness in-depth measurements and microstructure analysis, and from the blocks, the test specimen for the tensile and LCF-tests are manufactured. To record the properties of the material near the surface relevant for the deep rolling process, these samples are taken as close to the surface as possible. The samples are manufactured in accordance to the standards EN ISO 6892-1 [60] and ISO 12106 [61]. The used geometries of the specimens are shown in Fig. 5.

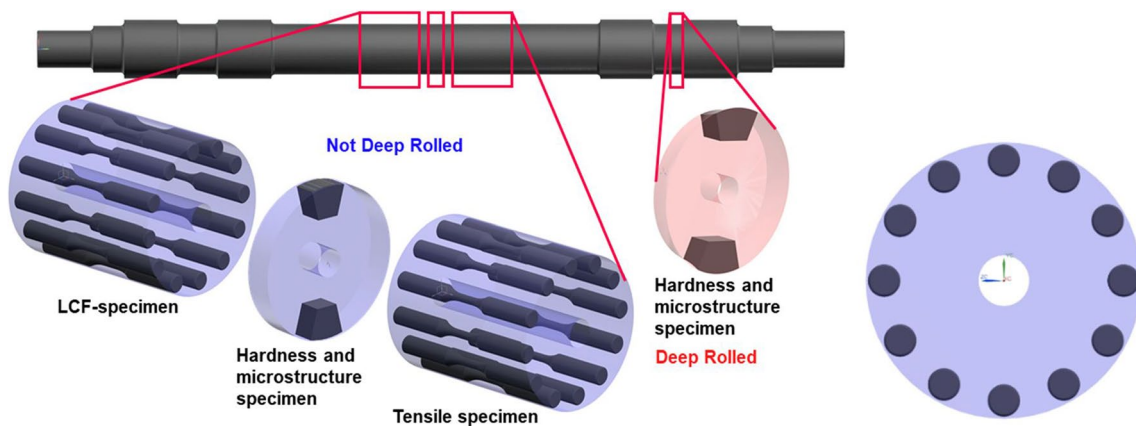


Fig. 4 Schematic specimen location of the railway axle from which they are machined

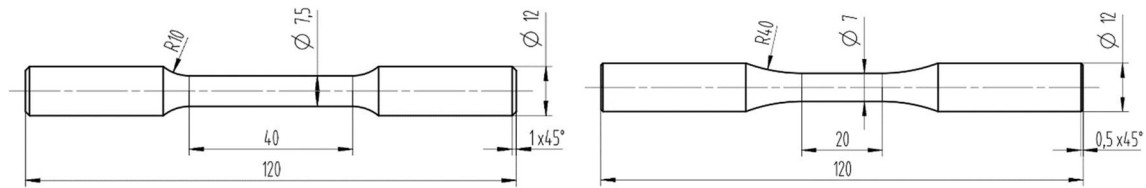


Fig. 5 Tensile (left) and LCF (right) specimen geometry

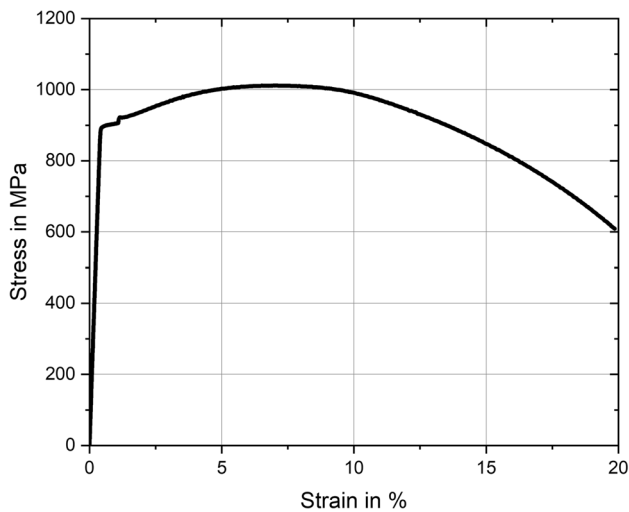


Fig. 6 Monotonic stress strain behaviour of the base material

Table 2 Monotonic tensile test results

Monotonic properties	Symbol	Unit	Mean value
Young's modulus	E	MPa	217,836
Yield stress	$R_{p0.2}$	MPa	902
Ultimate tensile stress	R_m	MPa	1,015
Elongation	A	%	19

are used to investigate the sensitivity of the material to an increased strain rate. When the strain rate is elevated, an increase in the yield strength $R_{p0.2}$ from 24 to 47 MPa and an increase in the tensile strength R_m from 13 to 32 MPa is observed. Young's modulus E and elongation A remain in the same range. From these test results, it is concluded that the material is sensitive to the influence of the strain rate, but the effect is comparably minor. Therefore, the influence of strain rate can be simplified neglected in the further investigations.

Experimental investigations

Tensile test

Tensile tests are performed according to EN ISO 6892–1 [60]. Six quasi-static tests and five tests with an increased strain rate from 0.0267 s^{-1} to a maximum of 0.2 s^{-1} are performed. The tests are performed at a uniaxial Instron testing machine with a nominal force of $\pm 100 \text{ kN}$. The control is provided by the Instron FastTrack 8800 controller and the strain is recorded using an Instron extensometer with a gauge length of 37.5 mm. The geometry of the specimen shown in Fig. 5 (left) is used. The six quasi-static standard tests provide similar results. Figure 6 shows graphically the stress–strain result of a representative experiment, while in Table 2 the resulting mechanical material properties are listed. The mean values of the six performed tests are provided. The comparison with the test results published in [62, 63] with the same material, but samples manufactured from bars with a smaller diameter and without going through the previous manufacturing process of the railway axle, shows similar results.

During deep rolling, the material is loaded at high deformation rates. Tensile tests with increased strain rates

Cyclic investigations

Cyclic material behaviour is investigated with the same testing machine and control as the tensile tests. The used Instron extensometer has a gauge length of 12.5 mm and the used specimen geometry is shown in Fig. 5 (right).

A total of ten standard LCF tests according to ISO 12106 [61] and five additional tests, including tests specific to deep rolling, are carried out. Standard tests are performed strain-controlled with a strain rate $\dot{\epsilon} = 1\%/sec$ and an R-ratio $R_\epsilon = -1$. The following strain amplitudes \mathcal{E}_a are applied: 0.25%, 0.3%, 0.35%, 0.4%, 0.45%, 0.5%, 0.7%, 1.0%. Figure 7 (left) shows exemplary the result of the cyclic stress–strain relationship of the test with a strain amplitude of 1.0%. The first, second, fifth, 10th, and 30th cycles are shown.

Figure 7 (left) and (right) show that the material demonstrates cyclic softening behaviour. The Bauschinger effect is dominant [64]. The yield stress decreases rapidly with increasing accumulated plastic strain and stabilizes at a nearly constant level, compare to results in Fig. 7 (right).

Compared to the existing literature [62, 63] the result shows a similar behaviour, but lower resulting stress values, about 100 MPa. The reason is probably the material history,

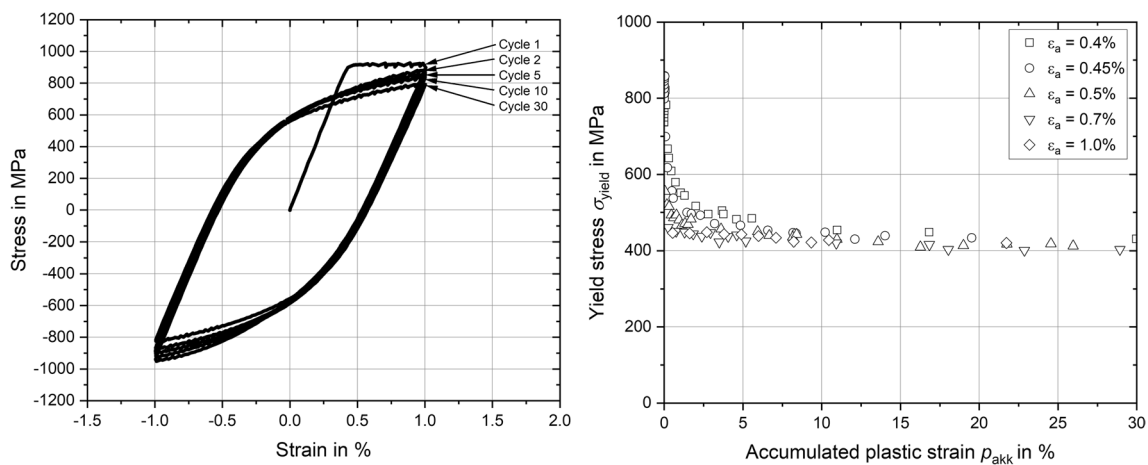


Fig. 7 LCF test result with applied strain amplitude of 1% (left); Evaluation of the cyclic yield stress decrease plotted versus the accumulated plastic strain (right)

the manufacturing process and the size of the workpiece from which the samples were taken.

In addition to standard LCF tests, additional specific cyclic uniaxial tests are carried out. These were defined based on evaluations of previous results of the deep rolling simulation model presented in this publication. The first test reproduces the occurring at the surface and the second below the surface. Large strains appear on the surface and large accumulated plastic strains due to the repeated contact with the tool. The strain-controlled test starts with an applied load in the compression direction up to a strain of 1%, followed by 100 cycles at $R_\varepsilon = -1$ and $\varepsilon_a = 1\%$ and then an applied tensile strain of 10%. The test result is shown in Fig. 8 (left). The comparison of the initial load in tension or compression shows very small differences and the stress–strain behaviour is almost identical. The second test, Fig. 8 (right), represents the behaviour below the surface. The test starts again

in compression up to a strain $\varepsilon_a = 0.45\%$, low plasticizing occurs, and then it changes to tensile loading. The tests are carried out to validate the material model presented in Section "Material model".

Microstructure analysis

To analyse the microstructure, the prepared specimens were inspected with the Zeiss Axio Observer Inverted optical microscope. Figure 9 (left and middle) shows the comparison of the images obtained at $1000\times$ magnification, deep rolled (middle) and untreated (left). Additionally, the region up to $5\ \mu\text{m}$ has been marked with red lines. Close to the surface, a change in the surface is visible. To obtain a finer resolution, the deep rolled sample is observed under a scanning electron microscope (SEM). The SEM Zeiss (Leo) with Tungsten Filament is used. The image is magnified 3000

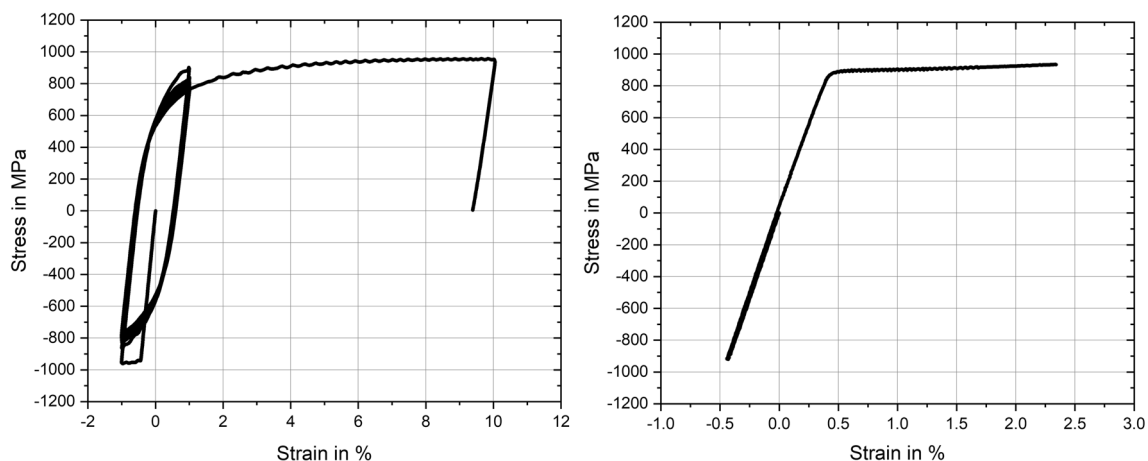


Fig. 8 Deep rolling specific uniaxial cyclic test result representative for the happening at the surface (left) and representative for the happening under the surface (right)

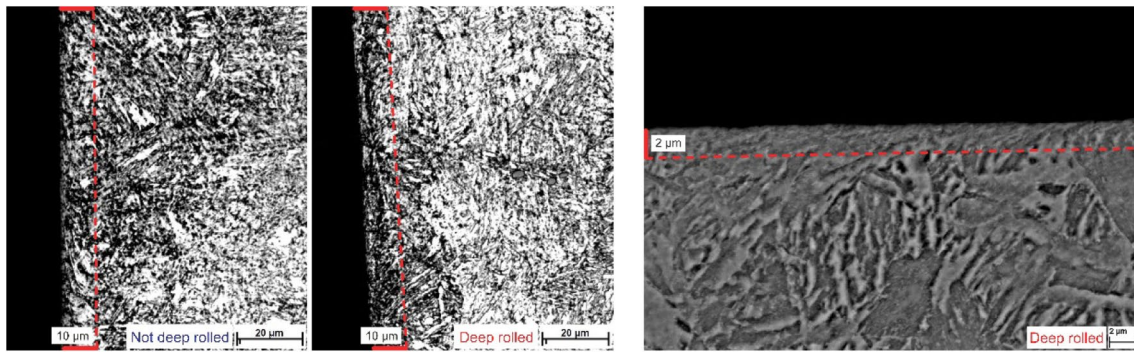


Fig. 9 Results of the microstructure analysis resulting from the optical light microscope (left and middle) and the SEM (right)

times. The result is shown in Fig. 9 (right). In a range up to approximately 3 μm to 4 μm, the changed microstructure is recognizable. The microstructure is distorted as a result of the plastic deformation that occurred during the application of the deep rolling process. As reported in [8, 15, 20, 42] the microstructure change is material dependent and very local. A very thin layer with a depth of several μm is typical, proven here.

Hardness measurements

Numerous hardness measurements were executed on the railway axle, at the surface and in-depth. Surface measurements are made with the EMCO-TEST M4C universal hardness testing machine and in-depth profiles are made with a ZwickRoell DuraScan 80 hardness testing machine. The tests were carried out taking into account the standards DIN EN ISO 6506 [65] and DIN EN ISO 6507 [66]. The test procedures Vickers HV10, HV1 and Brinell HBW2.5 are performed for the surface measurements. In-depth measurements are conducted using Vickers HV1 up to a depth of

7 mm and HV0.05 up to 0.9 mm, results visible in Fig. 10 (left) and (right). For a better illustration of the measurement trends, the measurement values are fitted with a 2nd order polynomial approach, additionally the standard deviation is shown. For each measurement, comparative tests are performed between deep rolled and nontreated sections. All results reveal lower or similar hardness. The surface measurements HV10 show an averaged hardness reduction from without treatment to deep rolling treated from 314 to 307, for HV1 from 345 to 315 and for HBW 2.5 from 287 to 284.

In [8, 16] it is mentioned that quenched and tempered steel materials, such as 34CrNiMo6, exhibit the lowest hardness increase potential after deep rolling. The decrease in hardness during deep rolling of this material can be related to the softening behaviour visible in the LCF test results, Section "Cyclic investigations".

Roughness measurement

Using the Taylor Hobson Surtronic Duo portable roughness tester, the surface roughness value Ra is determined in

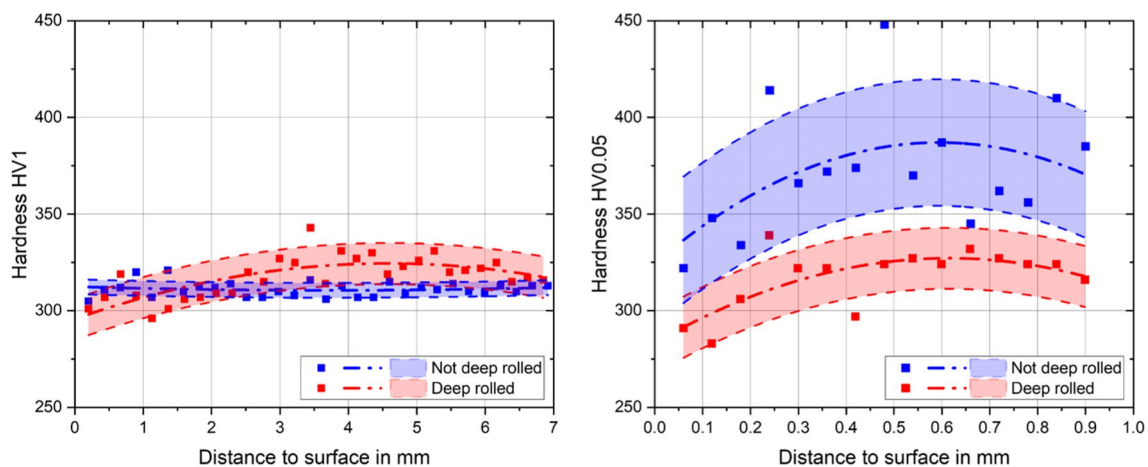


Fig. 10 In-depth hardness measurement results measured with HV1 (left) and HV0.05 (right)

seven deep rolled sections and five not deep rolled sections of the railway axle. By applying the deep rolling process, the roughness of the surface is reduced from $R_a 0.548 \mu\text{m} \pm 0.04$ to $R_a 0.321 \mu\text{m} \pm 0.06$. According to DIN EN 13261 [55] the measured roughness is below the allowed roughness limits before and after deep rolling.

Residual stress measurement

The residual stresses are determined using the measuring methods recommended in DIN EN 13261 [55] for the measurement of railway axles, i.e. the hole drilling method (HD) method and the X-ray diffraction method (XRD). Since the measurement methods have measurement process caused deviations, these are considered in the measurement results and explained below.

Hole drilling method (HD)

The residual stress measurement by the HD method is performed with a Sint Technology MTS 3000 – Restan, considering ASTM E837 [67]. For the measurement, a three-radial grid strain gauge rosette is glued on the railway axle. After positioning the measuring system, a small hole with a diameter of 1,6 mm is drilled in the provided centre of the rosette. To avoid induction of new residual stresses, the drilling is performed with a special driller which is driven by a high-speed air turbine which rotates at up to about 70,000 RPM and is fed in 0.05 mm increments. The strain gauge measures the relaxation of the residual stresses caused by the occurring hole. The residual stresses are calculated from the measurement system from the measured strains [68]. For the investigated railway axle, one measurement, MP4, in the deep rolled section, is measured up to a depth of 1 mm. If stresses near or above the yield stress occur during the measurement, they must be corrected as a result of local

yielding around the hole as the stresses are overestimated by the measurement, details see [69–71]. Figure 11 shows the measurement results up to a depth of 1 mm. The stress values with a ratio of

$$\frac{\sigma_{measured}}{R_{p0.2}} \cdot 100 > 65\% \quad (1)$$

are corrected as recommended in [70]. The measurement results up to a depth of 0,2 mm are neglected, due to the limited measuring accuracy of the measuring method in this range. The measurement points and the mean value of the measurement value are plotted. In addition, the measurement deviation with superimposed considered a typical and conservative measurement repeatability of $\pm 2\%$ [72, 73] is drawn.

X-ray diffraction method (XRD)

Residual stress measurement with X-ray technology is performed with a Stresstech XStress 3000 G2. Using Cr K α X-ray radiation, an irradiated spot of 3 mm is irradiated for 10 s without using a filter. The measurement is evaluated using the cross-correlation calculation method and the $d(\sin^2 \psi)$ evaluation method [74, 75]. This measurement method evaluates the residual stresses a couple of μm below the surface [76, 77]. To measure in depth, the material must be removed. To avoid a modification of the residual stresses due to the removal-manufacturing-process itself, the material is primarily removed by electrochemical polishing. The in-depth profile is achieved in increments of 0.25 mm followed by repeated measurements. Two measurements are made up to a depth of 2 mm, MP2 and MP3, and one measurement up to 8 mm, MP1, on the investigated railway axle in deep rolled sections.

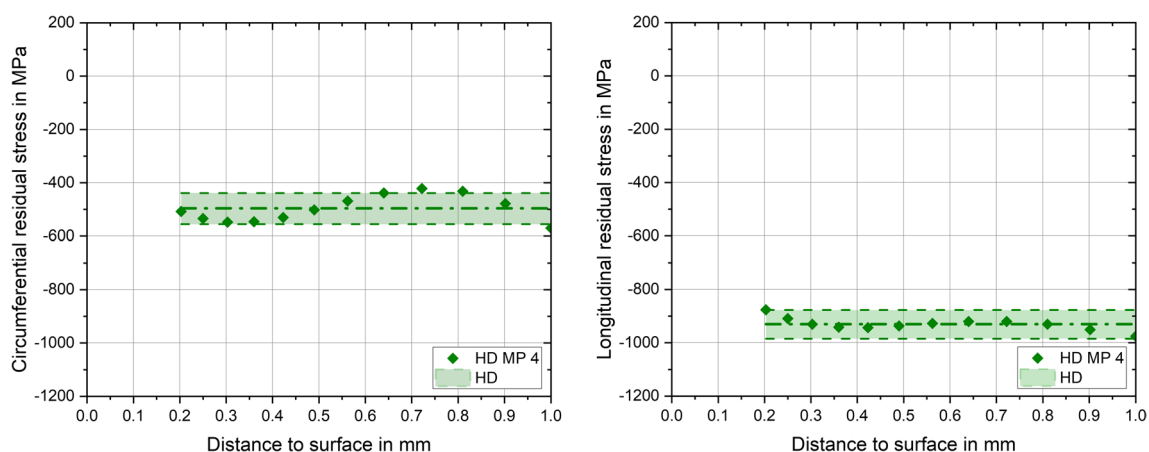


Fig. 11 Circumferential (left) and longitudinal (right) hole drilling residual stress measurement results

In Fig. 12 the measurement results of the individual measurement points are shown with dots. Up to 2 mm, the mean and standard deviation of the measurement results are calculated. The mean value and the smoothed measurement curve larger than 2 mm of the deeper measurement are connected and plotted. Additionally, a scatter band is plotted, this is composed of the sum of the standard deviation, the repeatability of the measurement procedure, and the averaged measurement deviation.

Full width at half maximum (FWHM)

Another essential measurement parameter is strain hardening [9]. The strain hardening can be identified by FWHM (Full Width at Half Maximum), additionally resulting from the XRD measurement. The FWHM value is a measure of the dislocation density, grain distortion and type II micro residual stresses. Strain hardening cannot always be detected

by microhardness measurements [12, 43, 78, 79], as also occurred in this study. In Fig. 13 the results of the FWHM measurement are shown in circumferential (left) and longitudinal (right) directions. The measured values indicate a high FWHM value, and thus a strain hardened condition at the surface. Subsequently, the values decrease and stabilise at a depth of approximately 4 mm to constant values. This is the depth up to which the near-surface material is strain hardened by the application of the deep rolling process.

Finite element simulation

Deep rolling simulation model

An implicit 3D deep rolling simulation model is built in the commercial finite element simulation software MSC Marc 2020. The model is built to include all deep rolling

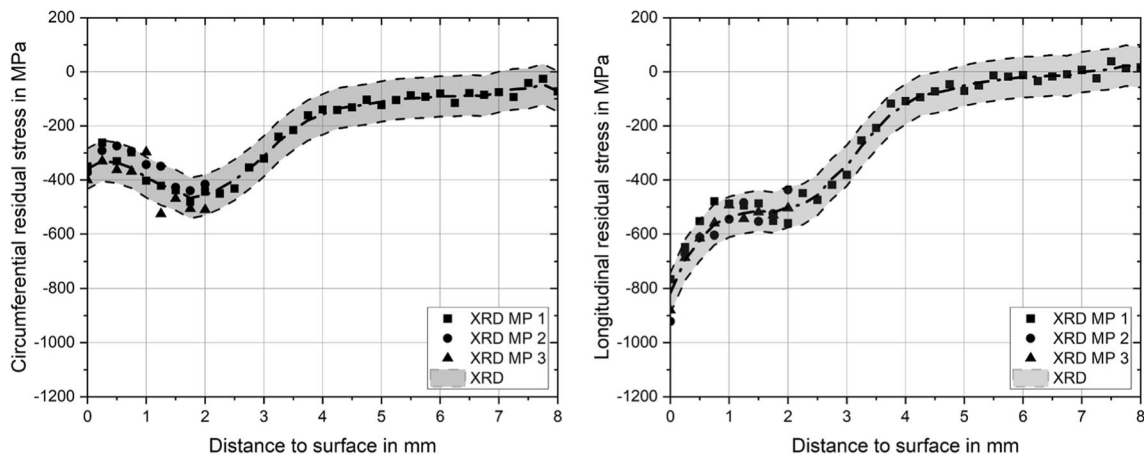


Fig. 12 Circumferential (left) and longitudinal (right) XRD residual stress measurement results

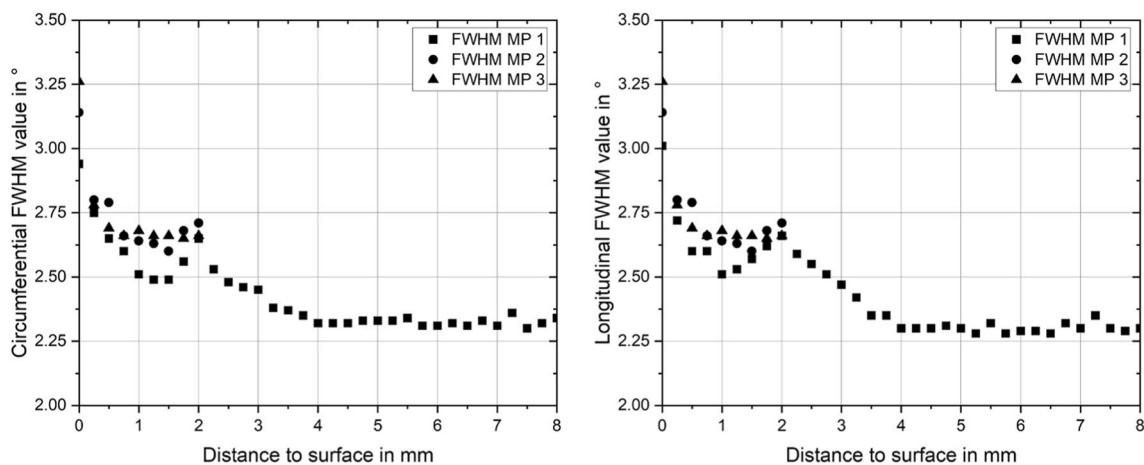


Fig. 13 Circumferential (left) and longitudinal (right) measured FWHM values at 3 measurement points (MP)

influences and parameters identical to those used in real deep rolling of the railway axle as described above. The model consists of a representative flat model and deep rolling tools. Main numerical challenges are the three occurring nonlinearities: the contact, material model and occurring large strains.

Representative flat model and deep rolling tools

The treated railway axle is modelled as a flat block in order to reduce the computation effort and enable an efficient simulation procedure to investigate several process parameters. The influence of the surface geometry is investigated based on a model with adapted geometry. Due to the comparably large diameter of the railway axle, the difference in the determined residual stress depth profiles is limited. The transferability of the results by the representative flat model to real railway axle application is presented in detail in Section "[Transferability of results to real railway axle application](#)". Therefore, the surface curvature is neglected in the simulation in the first place, which is in line with a previous work in [43]. This simplification leads to an efficient

simulation model exhibiting significantly reduced computing time, which is important for comprehensive sensitivity studies in the future.

The symbolic cut-out of the numerical model from the railway axle geometry is depicted in Fig. 14 (top left and top right). The representative flat model, visible Fig. 14 (below right) is meshed by 8-node hexahedral elements with linear shape functions. The block has dimensions of 36.6 mm in X-, 45.2 mm in Y- and 21.9 mm in Z-direction. The X-direction is defined positive in the rolling direction of the tools, which corresponds to the circumferential direction of the railway axle. The longitudinal orientation equals the Y-direction in the simulation, which is defined positive in the feed direction. The Z-direction is defined positive from the surface to the inner of the meshed block, the radial direction of the axle.

The area in the middle of the flat model, which is in contact with the deep rolling tools, is evenly finely meshed. By a mesh sensitivity analysis, the size of the mesh is defined. The used mesh size is a compromise between the ability to guarantee convergence in this contact calculation and the simulation time, which strongly depends on the

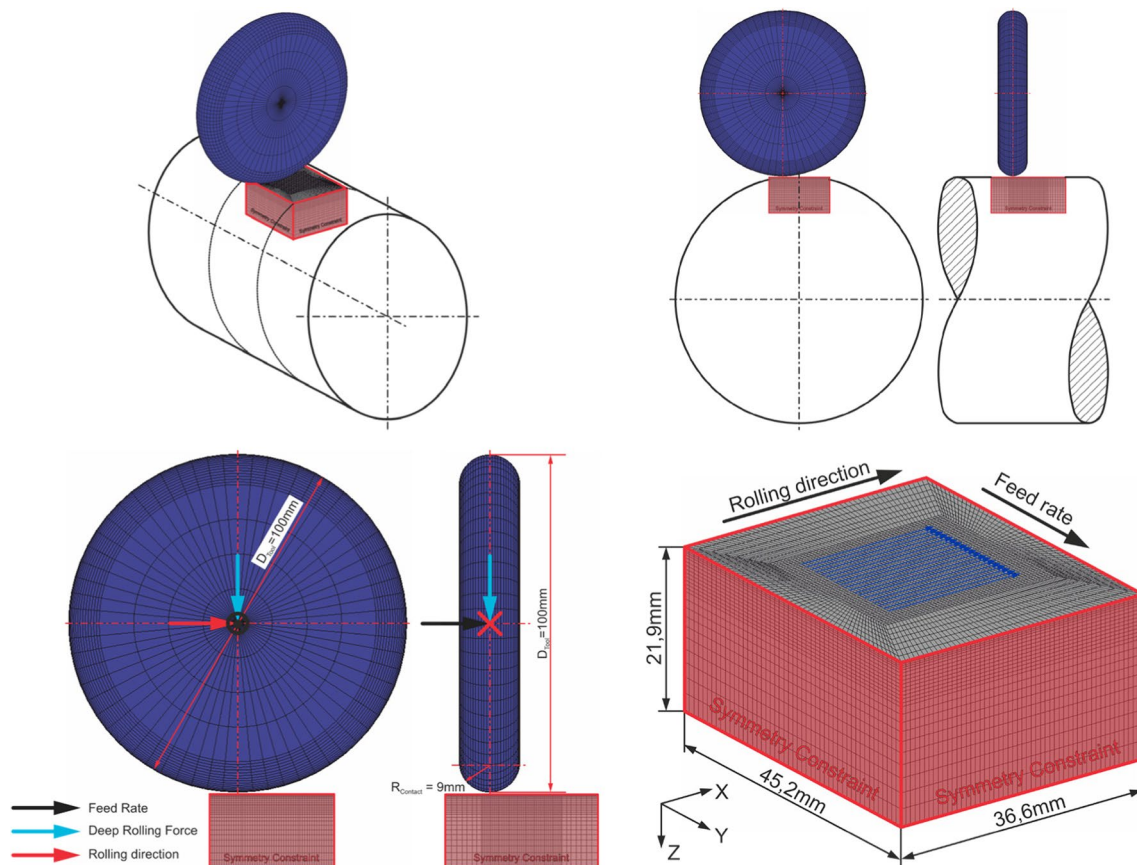


Fig. 14 Symbolic illustrated location of the simulation model in the railway axle geometry (top left and right), numerical deep rolling simulation model with marked tool dimensions, applied loads and constraints (below left) and representative flat model (below right)

number of elements. The elements on the surface exhibit a dimension of $0.5 \times 0.5 \times 0.25$ mm. The deep-rolled area is surrounded by a connecting area to the constraints. There, the mesh can be coarser to reduce simulation time ensuring same accuracy of the results in the regions of interests. The required dimensions of the connecting area, thus also the dimensions of the flat block, and the required element size in Z-direction direction are defined again by sensitivity analysis. In the performed sensitivity analyses, starting from a larger model with introduced uniform residual stress field in all directions in the centre of the simulation model, one dimension of the model or mesh property is changed at a time and its explicit influence is evaluated. The aim is to reduce the dimensions and therefore the number of elements to an acceptable minimum without compromising the residual stress result in the centre of the simulation model still achieving a uniform introduced residual stress field. The effort is done to reduce the simulation time associated with the number of elements to a minimum and to enable further fundamental deep rolling parameter sensitivity analyses with the presented model. The clamping of the simulation model is done on all sides, except the contact surface, with symmetry conditions.

Disc tools are used to deep roll the railway axle. They are made of a significantly stiffer material compared to the railway axle steel. Therefore, the deep-rolling tools can be modelled in the simulation as analytically described rigid bodies. [43, 44, 80] The tools have a diameter $D_{Tool} = 100$ mm and a contact radius $R_{Contact} = 9$ mm, as in reality and listed in Section "Deep rolling process", and are visible in Fig. 14 (below left). Each tool is controlled by a central node.

Simulation procedure

The feed rate is modelled in the simulation by several parallel-arranged tools. Due to the fact that two opposite-arranged tools and a feed rate of 0.5 mm/rev are used for the deep rolling of the railway axle, in the simulation, the half feed rate, 0.25 mm/rev, must be considered. The feed rate is modelled by the distance between the tools arranged in parallel. The feed rate of 0.25 mm/rev equals a gap of 0.25 mm.

Figure 15 (left) shows the deep rolling paths symbolically presented with blue arrows. As in reality, the tools deep roll the surface one after the other. Initially, the deep rolling force is applied to the first deep rolling tool step by step, visible in Fig. 15 (right). The tool contacts the representative flat model and when the force is fully applied, the controlling centre node of the tool is displaced along the rolling direction. Due to the defined friction contact between the tool and the meshed block, the tool rolls over the surface. The typical steel to steel friction coefficient $\mu = 0.1$ is used, see also [81–83]. According to [84] it is important to use a certain friction value, but its magnitude generally plays a minor role. After reaching the end of the deep rolling path, the deep rolling force is reduced again to zero. While the first tool is deep rolling the surface, the deep rolling process of the second tool starts at such a defined distance that the following tool does not influence the previous contact calculation and vice versa. This allows the reduction of simulation time. Following the same sequence, a total of 80 tools roll over the surface of the representative model. The continuous superimposed displacement of the tools in the feed direction, as occur in reality due to the simultaneous rotation of the railway axle and the continuous applied feed rate to the tool,

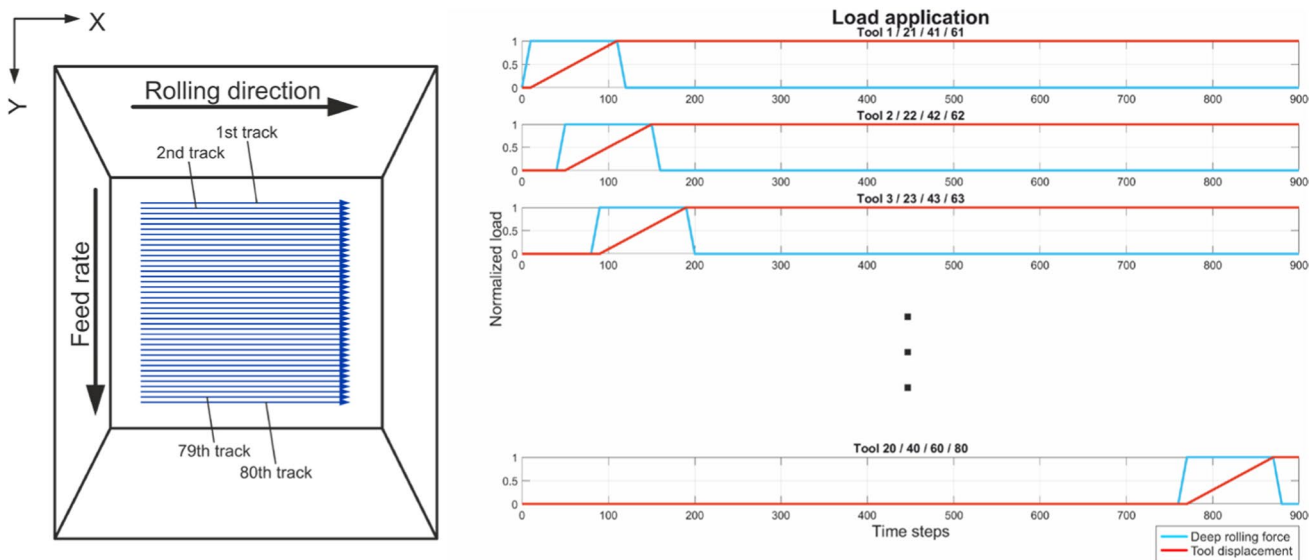


Fig. 15 Symbolic simulation procedure (left) and load application (right)

is neglected in the simulation. The displacement converted to the deep rolling track length used in the simulation is very small and has neglectable influence on the simulation result.

Material model

To simulate the resulting residual stresses after deep rolling, the elastic–plastic material behaviour must be considered. This describes the relationship between stress and strain. Compromises must be made in the selection of the material model with regard to the computing time, the memory requirements and the implementation in the software used. For this purpose, the Chaboche material model implemented in MSC Marc 2020 is used. This model is a time-independent cyclic plasticity model. The model combines isotropic hardening and the nonlinear kinematic hardening rule [85]. Details of this material model can be found in [51–53].

The model is thus able to predict cyclic hardening or softening, but also the proper characteristics of cyclic plasticity like Bauschinger, ratchetting and mean stress relaxation effect, details on the effects are available in [64]. Based on the uniaxial experimental results presented in Section "Cyclic investigations" and described in [86], the material model is parameterised and thus the material behaviour is simulated realistically.

Figure 16 shows the evaluations used to parameterise the response of the model. The stress–strain cycles for which the kinematic parameters were optimised are shown in Fig. 16 (left). For parameter determination, the 30th cycle of the uniaxial test result is used, which is representative for the strain condition at the surface after deep rolling. The number of back stresses available in MSC Marc is limited to one. As a result, minor deviations in the area of re-yielding are noticeable, although it is attempted to keep these as low as possible. Figure 16 (right) shows the change in yield stress vs. accumulated plastic strain required for parameterisation

of the isotropic component. Care is taken to ensure that the rapidly softening behaviour is correctly represented at low accumulated plastic strain, important for the areas of low occurring plastic strain such as in the zero-crossing zone. The parameters were chosen in such a way that they can realistically represent areas with small and large plastic strains. During the deep rolling process application, a wide range of strains occur in the deep-rolled surface layer.

Figure 17 shows the experimental results presented in Section "Cyclic investigations". In addition, the stress response of the material model with the same applied strain to a single-element model is plotted. Single-element models are used to validate the calibration of the material model [23, 81]. Thereby one single element is modelled, the element is fixed at three sides with symmetry conditions and loaded in one direction. As a result, the stress–strain relationship of the material model can be evaluated. The comparison between the test results and the response of the material model is shown for the LCF test with $\mathcal{E}_a = 1,0\%$ (top left), the representative test of what happens at the surface (below left) and the representative of what happens under the surface (below right). The response of the material model to various applied strains up to a strain amplitude $\mathcal{E}_a = 4,0\%$ is shown in Fig. 17 (top right).

Electrochemical removal and consideration in the simulation

As already mentioned above, it is necessary to remove material to measure in-depth residual stress profiles with both common measurement techniques, HD and XRD. The HD method uses the removal to determine the residual stresses, instead it is not considered by the XRD method. The residual compressive stresses introduced at the surface by deep rolling must be balanced by an area of tensile residual stresses to achieve the equilibrium of stress in the

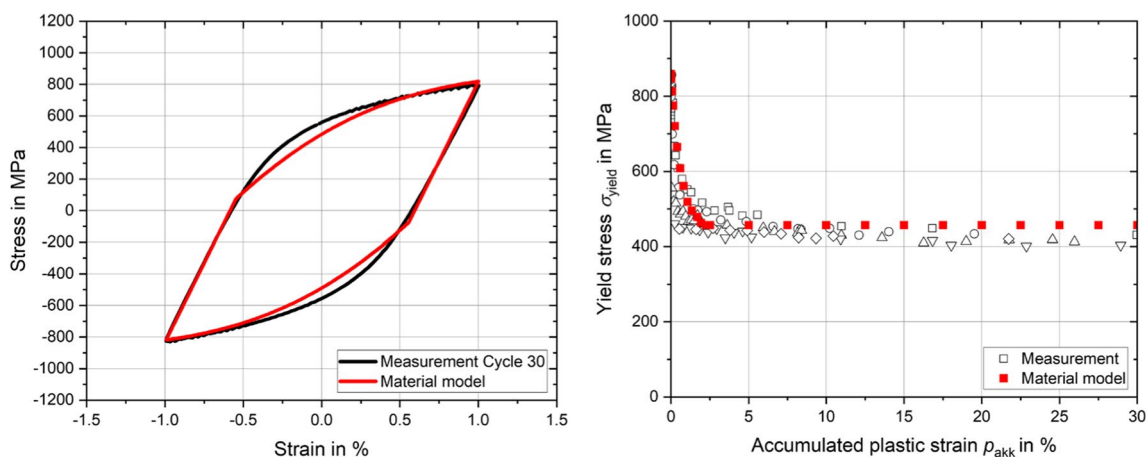


Fig. 16 Parameterisation of the kinematic (left) and isotropic (right) part of the Chaboche material model

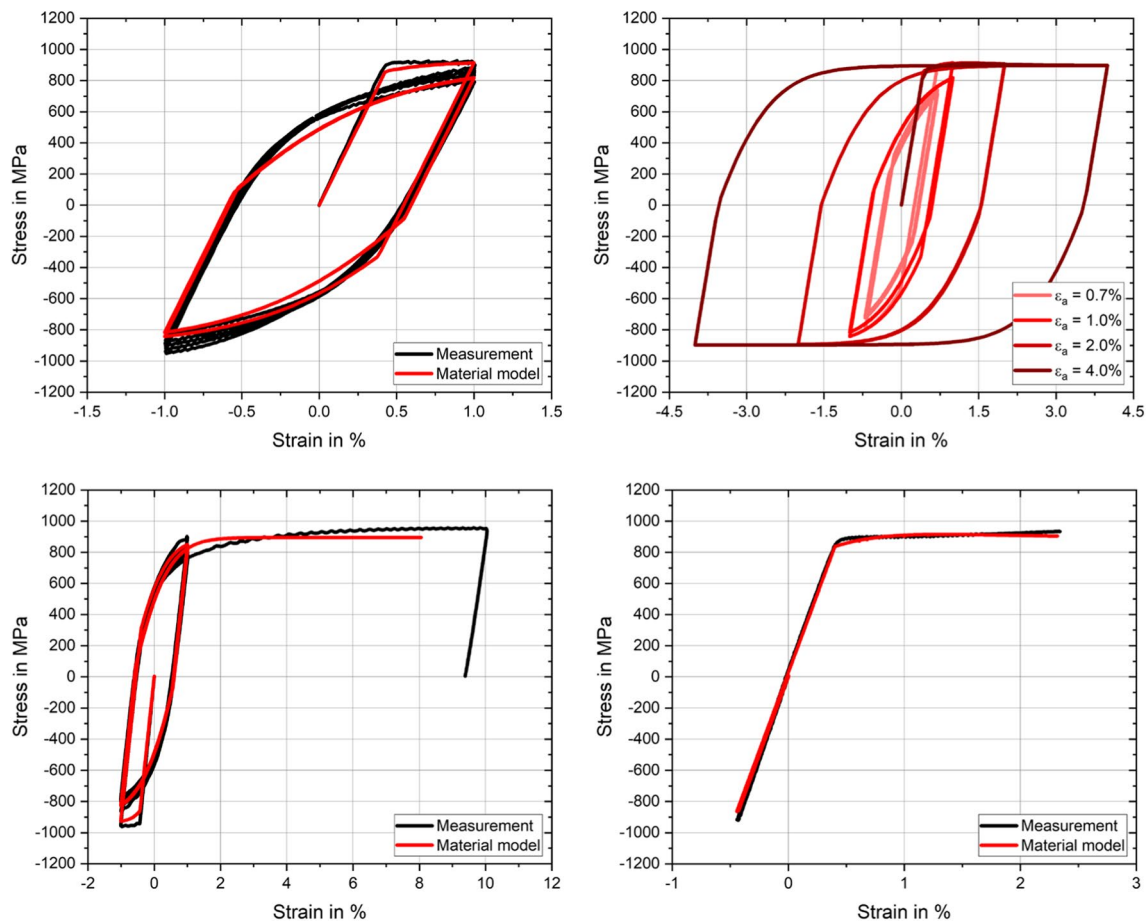


Fig. 17 Comparison of the test results and the material model response of the LCF test with $\varepsilon_a = 1,0\%$ (top left), the representative happening at (below left) and under (below right) the surface. Material model response to various applied strains (top right)

component. This is typically in an area below the surface. Due to material removal caused by the measurement process, the material with the highest prevailing compressive residual stresses is removed, naturally reducing the tensile residual stresses. As a result, as the hole depth increases, the tensile residual stresses approach zero and thus are not detectable by the XRD method. In Fig. 12 (left) and (right) this behaviour can be seen in the measurement results by XRD up to 8 mm.

Therefore, this measurement method cannot measure the actual stress profile that prevails in the component. The zero crossing and the position and level of the tensile residual stresses cannot be detected. There are three ways to determine the stress profile that prevails in the component:

- Analytical correction of the measurement result according to the theory of Moore and Evans [38]
- Correction of the measurement results with the help of FE and an arbitrary residual stress distribution [39]
- Simulation of the residual stress profile using FE and consideration of electrochemical polishing [39, 87]

Especially for residual stress curves with large maximum stress over the yield stress, steep gradients and large effective depth, as in the present case, the electrochemical removal has a significant influence. The first two approaches are limited to elastic stress relaxation. Since this assumption is therefore not acceptable for the present case, in this study the last and most suitable is chosen.

To validate the simulation with the XRD measurements, the corrected residual stress profile from the simulation must be compared with the measurement. The stress curve without considering the electrochemical removal corresponds to the residual stress curve present in the component. This curve is essential for further component design, where the residual compressive stress range, the depth of the zero crossing and the position and magnitude of the tensile residual stresses can be determined. As already mentioned, the tensile residual stresses are not measurable with the two applied measurement methods.

In the simulation, material removal is performed by stepwise suppression of the element layers. The hole created during electrochemical removal has a diameter of approximately

7 mm, Fig. 18 (left). In the simulation, visible in Fig. 18 (middle and right), the layer of elements with an approximately round geometry, also with a diameter of 7 mm, are excluded. By suppressing, as in theory during the measurements, no additional residual stresses are introduced. The stress change due to the suppression of the residual stress afflicted elements and the changing geometry is calculated. Between each step, the equilibrium state is determined. In the centre of the removed area, a depth curve is determined for each step. The XRD system measures a few micrometres below the surface. [77] Therefore for each step, the surface value and the first nodal value below the surface are averaged and the occurrence values are plotted in depth, presented in Section "Simulation".

Results and discussion

The results of the tensile tests, cyclic investigations, microstructure analyses, hardness measurements and roughness measurements have already been presented completely in Section "Experimental investigations" as these properties are mainly used as input or validation data for the numerical simulation. In this section, the main focus is laid on the residual stress state after deep rolling. In addition to the reduced surface roughness and strain hardening, the influence by local residual stresses is significant for the service life and is therefore of particular interest.

As described in Section "Experimental investigations", the residual stresses present in the component are determined using two different measurement methods and simulated using the finite element method as described in Section "Finite element simulation". Considering electrochemical removal in the simulation, it is possible to validate the simulation with the measurement.

Without taking electrochemical removal into account, the residual stress state prevailing on the railway axle is present. Thus, the non-measurable zero crossing and compensating

tensile residual stress range can be determined. The residual stresses present in this region are important for the design, they have to be superimposed on the operating loads and therefore there is a risk of failure in this region below the surface.

Measurement

The results of the residual stress measurement, HD and XRD, are already prescribed in Section "Residual stress measurement". The results of the two residual stress measurement methods provide partly deviating results. Significant compressive residual stresses are measured on the surface in the circumferential and longitudinal directions. The surface results show a good correlation, but the steep gradient measured in longitudinal direction by XRD is not confirmed by the HD method. Measured differences also occur in the literature. For example, in the investigation of deep rolled railway axles made of EA4T material presented in [43] as well as in [77, 88–90]. The suitability of the various residual stress measurement methods may depend on the properties of the material to be measured. Examples are the material under investigation, grain size, and geometry, as well as the investigated post-treatment. The residual stresses measured with the HD method tend to be more compressive than those measured with XRD.

In the circumferential direction, the stresses measured by HD method are slightly more compressive than those measured with XRD, the scattering bands overlaps partly. In the longitudinal direction, the stress values on the surface are equal. The HD measurement results remain constant up to the maximum measurement depth of 1 mm and do not decrease, while the XRD measurement values decrease directly below the surface. This decrease can be seen up to a depth of 1 mm. Below, up to a depth of approx. 2 mm, a plateau forms. The same behaviour can be seen in the XRD results presented in [43] and again does not occur in the HD measurement result. Therefore, a theoretical approach of the

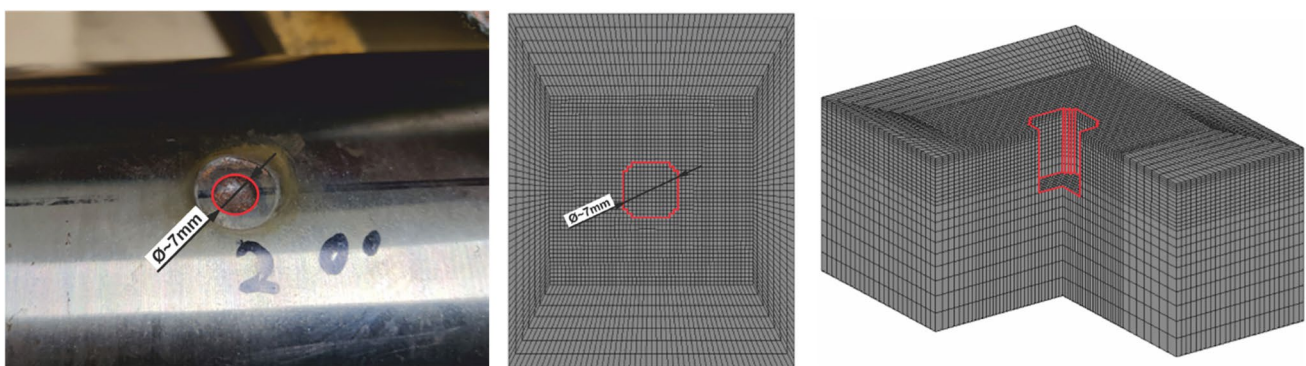


Fig. 18 Hole created by electrochemical removal (left) and consideration of the electrochemical removal in the simulation (middle and right)

combination of the two measurement methods is introduced. From the surface up to a depth of 1 mm the HD measurement results are considered and from 2-8 mm the XRD measurement results are used. The results are combined using a sixth order polynomial approach and by using the least squares method for the parameterisation. Figure 19 shows the measurement points used from the two measurement methods and the combined curve in the circumferential (a) and longitudinal (b) directions. In addition, the larger scatter range of the XRD measurement compared to the HD measurement was transferred and plotted for the entire depth.

Simulation

The developed deep rolling simulation model can be used to determine the residual stress state after deep rolling of the railway axle. Figure 20 shows graphically the simulation

procedure described in Section "Simulation procedure". From top left to bottom right the simulation progress and the introduced residual stresses are visible. Shown here are the von Mises stresses. The visible red dots at the front of the remaining residual stress region are the contact zones between the hidden tools and the representative flat model.

Figure 21 (left) and (right) show the graphical simulation result, depicted as von Mises stress plot.

The last imagine of the deep rolling sequence, Fig. 20 (below right) and Fig. 21 (left) show the same simulation result. To visualize the residual stress state in depth, a quarter of the simulation model is hidden, there. The introduced residual stresses near the surface and their reduction below the surface are visible.

The representative flat model dimensions, the deep rolling path length and the number of tools is selected in order to create a steady state evaluation area of consistent residual

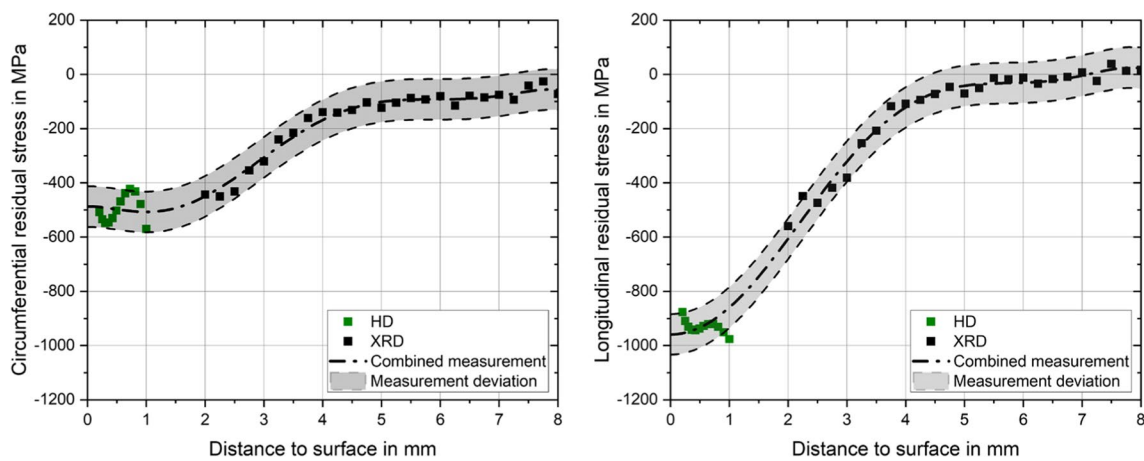


Fig. 19 Circumferential (left) and longitudinal (right) combined residual stress measurement results

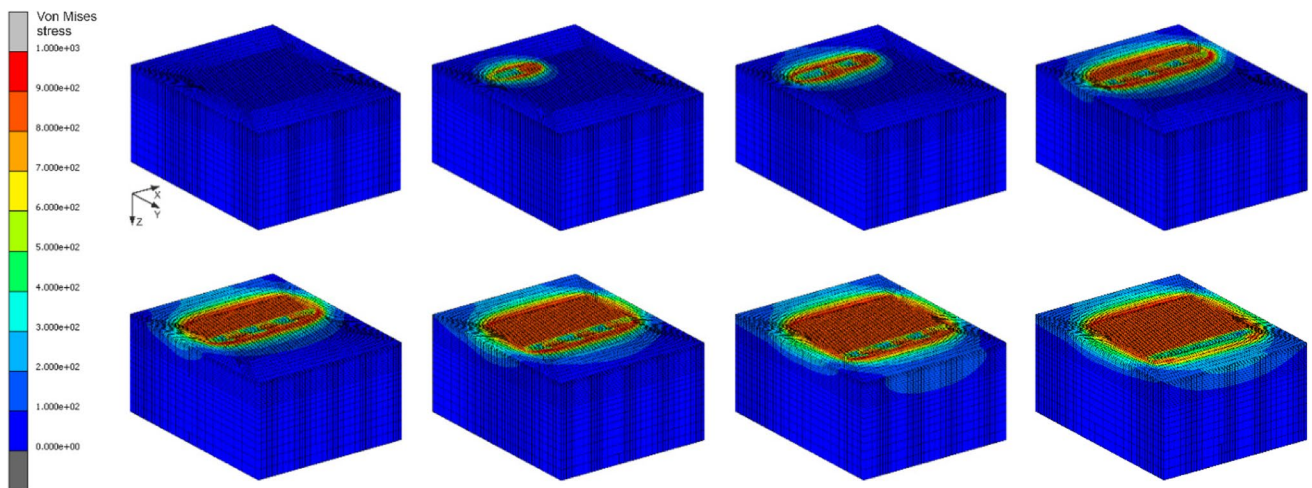


Fig. 20 Graphical sequence of the simulation procedure with visible generation of the residual stress state

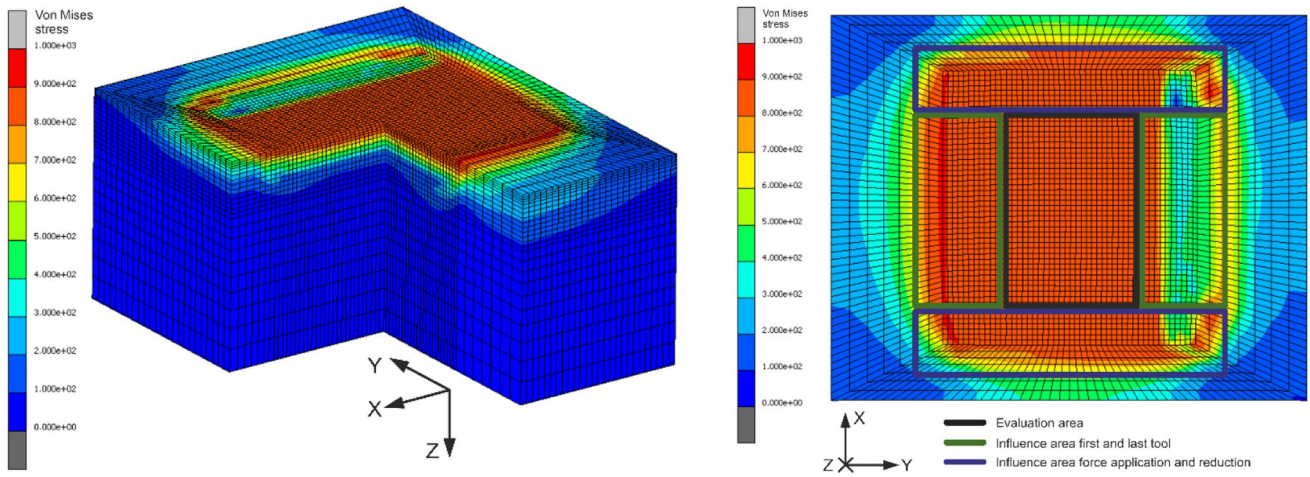


Fig. 21 Graphical deep rolling simulation result (left) and top view of the simulation result with marked influence and evaluation areas (right)

stresses in the middle of the simulation model, the marked evaluation area in Fig. 21 (right). This region is representative for the deep rolled condition at the railway axle. Surrounding this region, stress fields with large gradients are present. These results from the transition areas to the non-deep-rolled area. In X-direction, this is the area where the force is applied and reduced, respectively, the influence area of force application and reduction. The residual stress state in the Y-direction is strongly dependent on the subsequent deep rolling tools. Therefore, different conditions result in these surrounding areas, called the influence area of force application and reduction. These areas in the Y-direction are of great importance, because they occur also in the railway axle where the process application is started and stopped. Further investigations with the developed simulation model enable a closer look at these areas and allow their optimisation in the future.

The von Mises stresses illustrate the simulation result nicely, but are not suitable for the detailed examination of the introduced residual stress state. In their computation, the sign of the stress state is neglected. As already seen in the results of the residual stress measurements, however, the sign has a significant influence on the result and the further assessment. Figure 22 therefore shows the graphical simulation result with displayed circumferential stresses XX (left) and longitudinal stresses YY (right). Again, a quarter of the model is hidden to show the result in depth of the model. The figures are scaled the same. As desired, both results show an evenly distributed stress state in the middle of the representative flat model, the evaluation area. This area is again surrounded by unevenly distributed residual stresses in the so-called influence areas. The largest compressive residual stresses are noticeable near the surface, significantly more distinctive in the longitudinal direction.

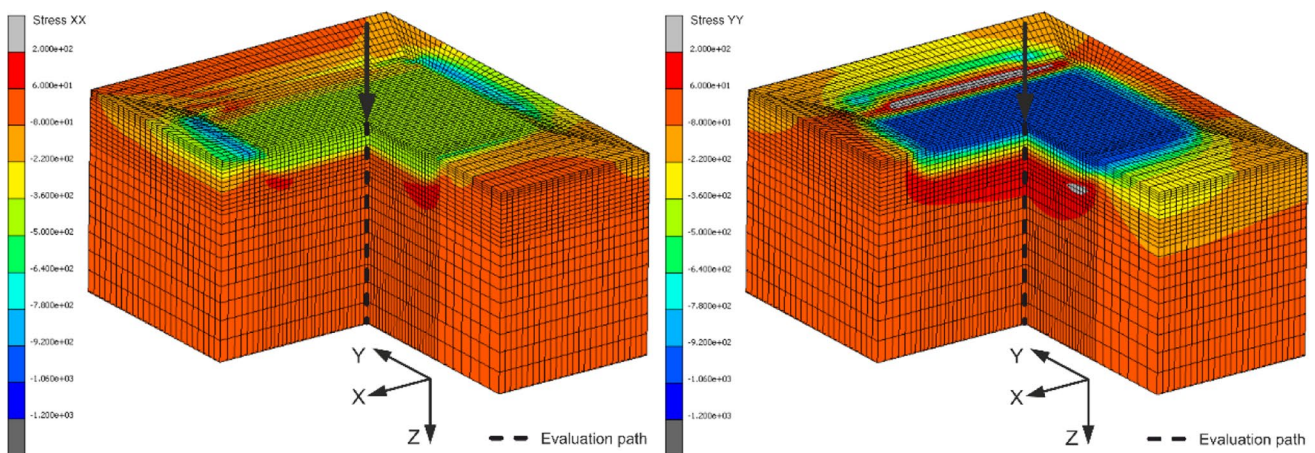


Fig. 22 Simulation result, visible are the circumferential (left) and longitudinal (right) stresses

Below this, the stresses reduce and change to a compensating tensile residual stress range. The stress distribution can be seen better if the stress curve is plotted over the depth.

To determine the residual stress depth curve, an evaluation path is selected in the middle of the simulation model and marked with the arrow in Fig. 22 (left) and (right). The stresses in the circumferential (left) and longitudinal (right) direction are evaluated and shown in Fig. 23. The solid line represents the stresses evaluated along the evaluation path. The dashed stress curve is obtained by considering the electrochemical removal described in Section "Electrochemical removal and consideration in the simulation".

Comparison of the measured and simulated residual stresses

To compare the results of the simulation with the results of the measurement, the in-depth simulation results considering

the electrochemical removal must be used, the dashed line in Fig. 23. The combined measurement results presented in Section "Measurement" are used for comparison. Individual measurement points are no longer shown for better clarity. In Fig. 24 the comparison of the measurement and simulation results is shown. It can be seen that both the circumferential (left) and longitudinal (right) residual stress curves show a good correlation.

Near the surface in the longitudinal direction, the simulation result is at the limit of the scatter range. There, the maximum occurring stresses are limited by the maximum tensile strength of the material. In the simulation, stresses higher than the maximum stresses considered by the material model occur in this range. This is possible because the von Mises criterion is used as the yield strength criterion in the material model. In the calculation of the von Mises stress, the hydrostatic stress state is neglected. Even low compressive stresses in the radial direction in combination

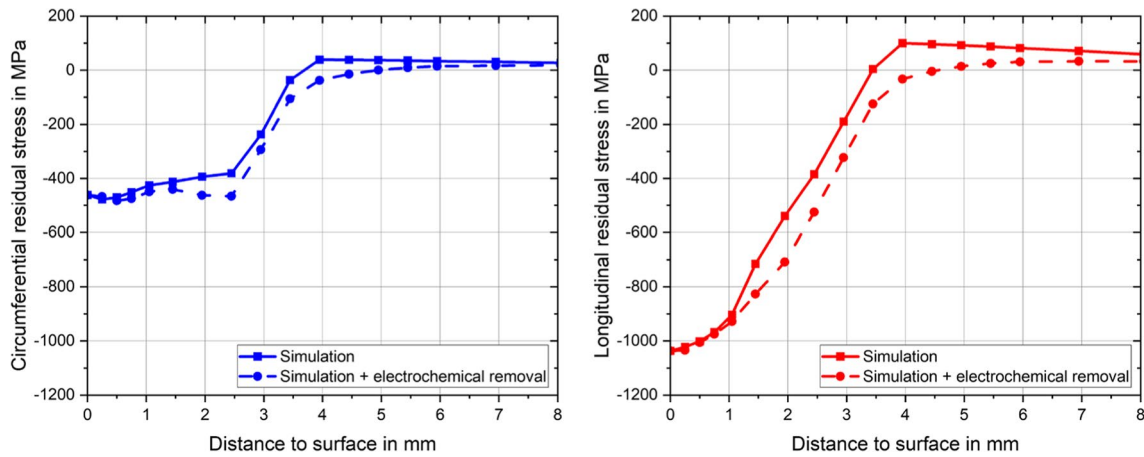


Fig. 23 Circumferential (left) and longitudinal (right) residual stress simulation results with and without numerical consideration of the electrochemical removal

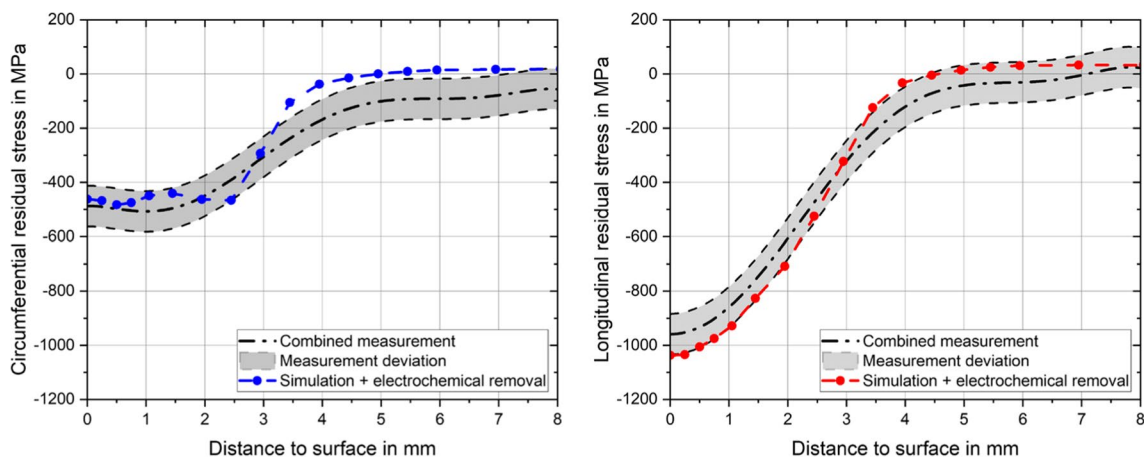


Fig. 24 Validation of the deep rolling simulation model with the simulated residual stresses after deep rolling with consideration of the electrochemical removal and the combined residual stress measurement results in circumferential (left) and longitudinal (right) direction

with high compressive stresses in the other two directions are sufficient to cause such a state and thus to achieve larger compressive stresses than the maximum stresses possible by the material model. Below that, the simulation results match the measurement results. Lower than 3 mm, minor deviations occur, such as those in the circumferential direction. These may be caused by residual stresses already present before the deep rolling treatment of the railway axle and the there decreasing depth impact of the process application.

As already mentioned above, the residual stresses present in the railway axle cannot be measured with the examined technologies. These can be determined using a validated deep rolling simulation model, as presented in this article. The residual stress depth curve resulting from the evaluation without considering the electrochemical removal represents the actually introduced residual stress state into the railway axle. The solid lines in Fig. 23 show this stress profile. In Fig. 25, these depth profiles are shown in one diagram in the circumferential, longitudinal and additionally in radial

directions. The highest compressive residual stresses of approximately -1,000 MPa occur in the longitudinal direction at the surface. Among, the stresses decrease steadily and reach zero crossing at a depth of about 3.5 mm. This is followed by the maximum of the tensile residual stress region of about + 100 MPa at a depth of 4 mm. In the circumferential direction, the compressive residual stress maximum of about -500 MPa occurs just below the surface. Stress decreases near the surface with a very slight gradient. At a depth of approx. 2.5 mm, the two profiles coincide and the circumferential stresses are reduced from this point onward with a steeper gradient, similar to the longitudinal stresses. The zero crossing occurs at a similar depth. Similarly, to the maximum compressive stresses, the maximum tensile residual stresses have approximately half the magnitude. The stresses in the radial direction are negligible in relation to the other two stress directions and bend around zero.

Transferability of results to real railway axle application

Finally, the transferability of the results based on the representative flat model to real railway axle application is investigated. Therefore, a simulation model with adapted outer contour of the railway axle is defined, see Fig. 26 (left and middle). The outer contour of the simulation model exhibits the full-scale railway axle diameter as the real railway axle in the sections where the residual stress measurements are performed. Instead of the Cartesian coordinate system, a cylindrical one is defined for this model. This facilitates the application of boundary conditions and the subsequent evaluation. The radial R-component corresponds to the Z-direction of the flat reference model and is positively defined from the surface to the inner of the model. The φ -direction is positively defined in the rolling direction of the tools, which equals the X-direction in the flat reference model. The Z-component corresponds to the longitudinal axis of the railway axle and is defined positive in feed direction of the tools, equal to the Y-direction used at the flat

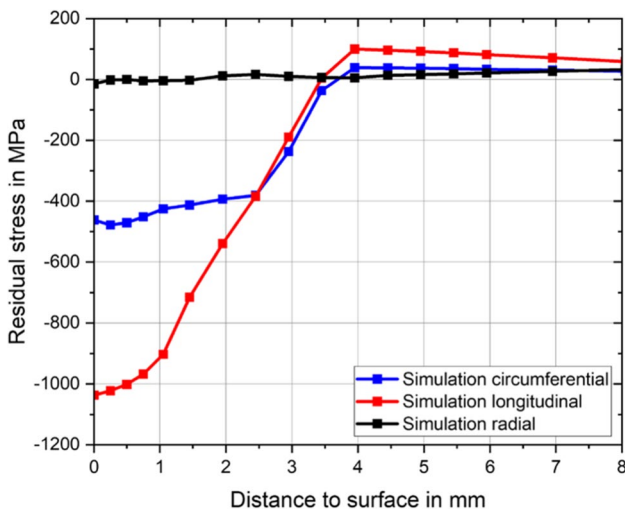


Fig. 25 Remaining residual stresses in the railway axle after deep rolling determined by finite element simulation

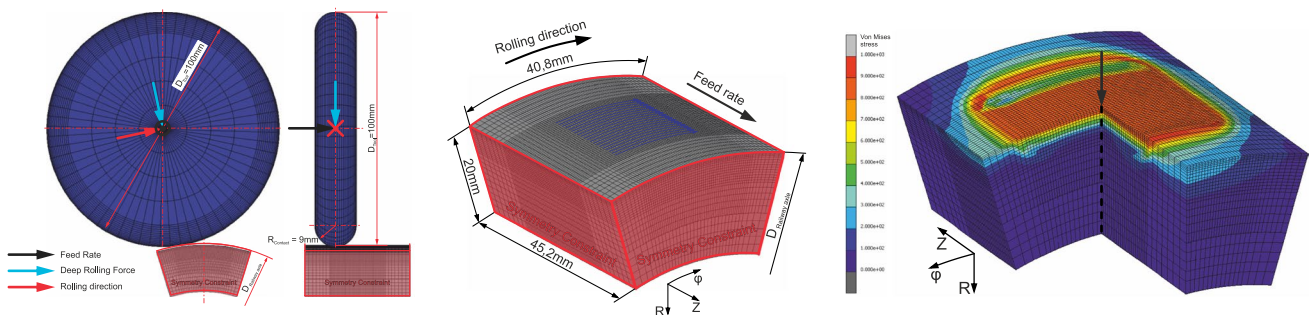


Fig. 26 Simulation model (left and middle) and graphical simulation result with marked evaluation path (right) with adapted outer contour to railway axle geometry

model. All other boundary conditions and the simulation procedure remain identical to the simulation model with flat representative simulation model.

In Fig. 26 (right) the graphical simulation result with marked evaluation path, for the residual stress in-depth evaluation used in Fig. 27, is shown. There, the comparison of the simulation results of the representative flat simulation model and the simulation model with railway axle geometry is presented in circumferential (left) and longitudinal (right) direction. The comparison of the in-depth residual stress distributions reveals that they are almost identical in the longitudinal direction and a minor difference is observable in the circumferential direction. Due to the already large diameter of the railway axle, however, the difference is limited. Since the applicability for a basic parameter investigation was considered during the development of a time-efficient simulation model, the computation effort is attempted to be kept within acceptable limits. By simplifying the numerical approach to the flat outer contour, one third of the computing time can be saved with good transferability of the results to real railway axle application.

Summary and conclusions

All main influences caused by deep rolling mentioned in [9] are investigated. With the combination of the experiments examined and the numerical simulation of the deep rolling process, it is possible to obtain a comprehensive overview of the effects caused by the deep rolling of the railway axle made of high-strength steel 34CrNiMo6.

The following list summarizes the main results:

- The results of the tensile test are similar in magnitude to those presented in the literature. The steel material 34CrNiMo6 shows low strain rate sensitivity.
- The material shows softening behaviour under cyclic loading. Uniaxial strain-controlled tests show lower resulting stresses compared to the literature results.
- A change in microstructure caused by deep rolling is detected only very locally up to a depth of $< 5 \mu\text{m}$.
- Neither at the surface nor at depth, an increase in hardness could be proven after deep rolling. The hardness remains at a similar level with a tendency towards slightly lower hardness.
- On the contrary to the hardness, strain hardening near the surface is detected by means of FWHM. The deep rolling treatment achieves surface FWHM values in the circumferential and longitudinal direction of more than 3° . Below the surface the values decrease and merge into the base material values of approx. 2.25° at a depth of 4 mm, the effective depth of the process application.
- Residual stresses are measured using XRD and the HD method. Comparable residual stresses are measured near the surface, but the two measurement methods differ significantly below the surface, especially in the longitudinal direction of the railway axle. The significant stress decrease below the surface determined by XRD cannot be confirmed by HD. As expected, the zero crossing and tensile residual stress range cannot be determined. The residual stresses approach zero, in both investigated directions, at a depth of approx. 5 mm.
- On the basis of the uniaxial tensile and cyclic material test results, a suitable Chaboche material model is parameterised and verified for the large range of occurring plastic strains during the deep rolling process application.

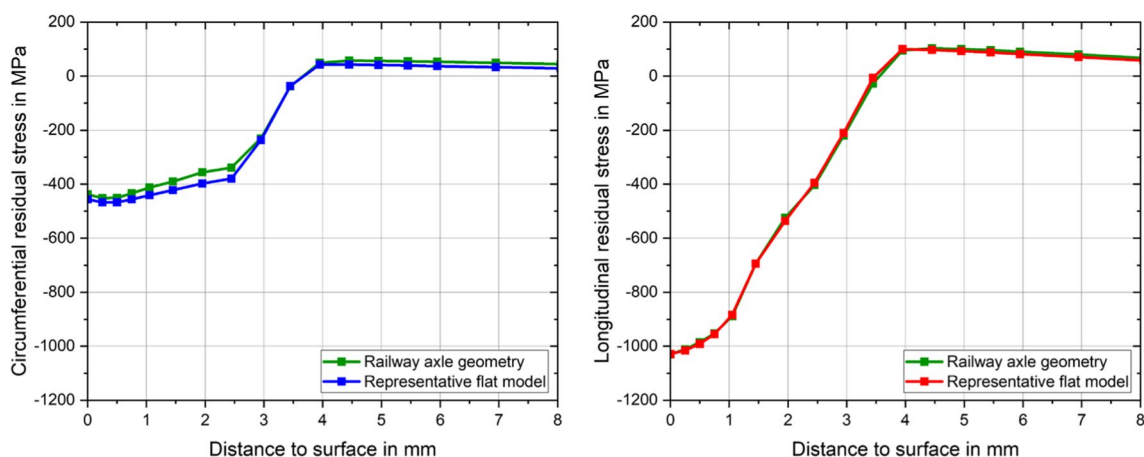


Fig. 27 Circumferential (left) and longitudinal (right) residual stress simulation results from the model with adapted outer contour to railway axle geometry and representative flat model

- A deep rolling simulation model has been developed. The Chaboche material model is added to the simulation model to allow the simulation of the residual stress state introduced by the process application. The electrochemical removal, required to measure in depth, is considered in the simulation.
- The simulation model is validated using combined results of the two applied residual stress measurements. The simulated depth profile shows good agreement over the entire depth.
- The maximum compressive residual stresses of approx. -1,000 MPa occur in the longitudinal direction near the surface, in circumferential direction maximally -500 MPa.
- Using the simulation model, the non-measurable, but for the design essential, zero crossing and tensile residual stress range below the surface can be determined. The zero crossing from the compressive to the tensile residual stress range occurs at a depth of 3.5 mm and the maximum occurring tensile residual stresses are approx. +100 MPa at a depth of 4 mm.

With the development of the validated deep rolling simulation model, the basis for the determination of the residual stress state in the near-surface region of the axle has been established. The simulation model can be used to investigate the influence of various deep rolling parameters on the residual stress state. Other materials can be considered with suitable material models. Furthermore, the groundwork is laid for digitally investigating railway axle-specific features in order to further integrate the deep rolling process into the railway axle design. A solid foundation for a future digital fatigue assessment of the railway axle and the possibility for further process optimisation is laid.

Funding Open access funding provided by Graz University of Technology.

Declarations The authors have no relevant financial or non-financial interests to disclose.

Conflict of Interest None.

Open Access This article is licensed under a Creative Commons Attribution 4.0 International License, which permits use, sharing, adaptation, distribution and reproduction in any medium or format, as long as you give appropriate credit to the original author(s) and the source, provide a link to the Creative Commons licence, and indicate if changes were made. The images or other third party material in this article are included in the article's Creative Commons licence, unless indicated otherwise in a credit line to the material. If material is not included in the article's Creative Commons licence and your intended use is not permitted by statutory regulation or exceeds the permitted use, you will need to obtain permission directly from the copyright holder. To view a copy of this licence, visit <http://creativecommons.org/licenses/by/4.0/>.

References

1. Betzold J, Pucelik J, Eisenberg S (2007) Eigenspannungen als Messgröße zur Qualitätssicherung: Residual stress as measured quantity in quality assurance. *Materialwiss Werkstofftech* 38(4):263–273. <https://doi.org/10.1002/mawe.200700133>
2. Rieger M, Moser C, Brunnhofer P, Simunek D, Weber F-J, Deisl A, Gänser H-P, Pippan R, Enzinger N (2019) Fatigue crack growth in full-scale railway axles – Influence of secondary stresses and load sequence effects. *Int J Fatigue* 132(2020):105360. <https://doi.org/10.1016/j.ijfatigue.2019.105360>
3. Simunek D, Leitner M, Maierhofer J, Gänser H-P, Pippan R (2019) Analytical and Numerical Crack Growth Analysis of 1:3 Scaled Railway Axle Specimens. *Metals* 9(2):184. <https://doi.org/10.3390/met9020184>
4. Ecoroll AG. Basic principles of deep rolling. <https://www.ecoroll.de/en/processes/deep-rolling.html>
5. Mahmoudi AH, Ghasemi A, Farrahi GH, Sherafatnia K (2016) A comprehensive experimental and numerical study on redistribution of residual stresses by shot peening. *Mater Des* 90:478–487. <https://doi.org/10.1016/j.matdes.2015.10.162>
6. Röttger K, Wilcke G, Mader S (2005) Festwalzen - eine Technologie für effizienten Leichtbau. *Materialwiss Werkstofftech* 36(6):270–274. <https://doi.org/10.1002/mawe.200500876>
7. Schulze V (2006) Modern mechanical surface treatment: States, stability, effects, Zugl.: Karlsruhe, Univ, Habil.-Schr, 2004. Wiley-VCH, Weinheim
8. Altenberger I (2005) “Deep Rolling - The Past, the Present and the Future”. University of Kassel, Institute of Materials Engineering, Monchebergstrasse 3, 34125 Kassel. Germany 2005:144–155
9. Delgado P, Cuesta II, Alegre JM, Díaz A (2016) State of the art of Deep Rolling. *Precis Eng* 46:1–10. <https://doi.org/10.1016/j.precisioneng.2016.05.001>
10. Hadadian A (2019) Finite element analysis and design optimization of deep cold rolling of titanium alloy at room and elevated temperatures. PhD Thesis. Concordia University, Montreal, Quebec, Canada
11. Gao J-W, Dai X, Zhu S-P, Zhao J-W, Correia J A.F.O., Wang Q (2022) Failure causes and hardening techniques of railway axles – A review from the perspective of structural integrity. *Eng Fail Anal* 141:106656. <https://doi.org/10.1016/j.engfailanal.2022.106656>
12. Hassani-Gangaraj SM, Carboni M, Guagliano M (2015) Finite element approach toward an advanced understanding of deep rolling induced residual stresses, and an application to railway axles. *Mater Des* 83:689–703. <https://doi.org/10.1016/j.matdes.2015.06.026>
13. Maierhofer J, Gänser H-P, Pippan R (2014) Prozessmodell zum Einbringen von Eigenspannungen durch Festwalzen. *Materialwiss Werkstofftech* 45(11):982–989. <https://doi.org/10.1002/mawe.201400276>
14. Regazzi D, Beretta S, Carboni M (2014) An investigation about the influence of deep rolling on fatigue crack growth in railway axles made of a medium strength steel. *Eng Fract Mech* 131:587–601. <https://doi.org/10.1016/j.engfracmech.2014.09.016>
15. Regazzi D, Cantini S, Cervello S, Foletti S, Pourheidar A, Beretta S (2020) Improving fatigue resistance of railway axles by cold rolling: Process optimisation and new experimental evidences. *Int J Fatigue* 137:105603. <https://doi.org/10.1016/j.ijfatigue.2020.105603>
16. Berstein G, Fuchsbaauer B (1982) Festwalzen und Schwingfestigkeit. *Z Werkstofftechnik* 1982(13):103–109
17. Huang J, Zhang K-M, Jia Y-F, Zhang C-C, Zhang X-C, Ma X-F, Tu S-T (2019) Effect of thermal annealing on the microstructure,

- mechanical properties and residual stress relaxation of pure titanium after deep rolling treatment. *J Mater Sci Technol* 35(3):409–417. <https://doi.org/10.1016/j.jmst.2018.10.003>
18. Beghini M, Bertini L, Monelli BD, Santus C, Bandini M (2014) Experimental parameter sensitivity analysis of residual stresses induced by deep rolling on 7075–T6 aluminium alloy. *Surf Coat Technol* 254:175–186. <https://doi.org/10.1016/j.surfcoat.2014.06.008>
 19. Schubnell J, Farajian M (2022) Fatigue improvement of aluminium welds by means of deep rolling and diamond burnishing. *Welding in the World* 66(4):699–708. <https://doi.org/10.1007/s40194-021-01212-1>
 20. Abrão AM, Denkena B, Köhler J, Breidenstein B, Mörke T (2014) The Influence of Deep Rolling on the Surface Integrity of AISI 1060 High Carbon Steel. *Procedia CIRP* 13:31–36. <https://doi.org/10.1016/j.procir.2014.04.006>
 21. Gharbi K, Moussa NB, Rhouma AB, Fredj NB (2021) Improvement of the corrosion behavior of AISI 304L stainless steel by deep rolling treatment under cryogenic cooling
 22. Muñoz-Cubillos J, Coronado JJ, Rodríguez SA (2017) Deep rolling effect on fatigue behavior of austenitic stainless steels. *Int J Fatigue* 95:120–131. <https://doi.org/10.1016/j.ijfatigue.2016.10.008>
 23. Perenda J, Trajkovski J, Žerovnik A, Prebil I (2015) Residual stresses after deep rolling of a torsion bar made from high strength steel. *J Mater Process Technol* 218:89–98. <https://doi.org/10.1016/j.jmatprotec.2014.11.042>
 24. Perenda J, Trajkovski J, Žerovnik A, Prebil I (2016) Modeling and experimental validation of the surface residual stresses induced by deep rolling and presetting of a torsion bar. *Int J Mater Form* 9(4):435–448. <https://doi.org/10.1007/s12289-015-1230-2>
 25. Chen S, Wang Z, Chakraborty A, Klecka M, Saunders G, Wen J (2020) Robotic Deep Rolling With Iterative Learning Motion and Force Control. *IEEE Robotics and Automation Letters* 5(4):5581–5588. <https://doi.org/10.1109/LRA.2020.3009076>
 26. Dänekas C, Heikebrügge S, Schubnell J, Schaumann P, Breidenstein B, Bergmann B (2022) Influence of deep rolling on surface layer condition and fatigue life of steel welded joints. *Int J Fatigue* 162:106994. <https://doi.org/10.1016/j.ijfatigue.2022.106994>
 27. Denkena B, Kroedel A, Gartzke T (2022) Process design of a novel combination of peel grinding and deep rolling. *Prod Eng Res Devel* 16(4):503–512. <https://doi.org/10.1007/s11740-021-01092-w>
 28. Maiß O, Denkena B, Grove T (2016) Hybrid machining of roller bearing inner rings by hard turning and deep rolling. *J Mater Process Technol* 230:211–216. <https://doi.org/10.1016/j.jmatprotec.2015.11.029>
 29. Tsuji N, Tanaka S, Takasugi T (2008) Evaluation of surface-modified Ti–6Al–4V alloy by combination of plasma-carburizing and deep-rolling. *Mater Sci Eng, A* 488(1–2):139–145. <https://doi.org/10.1016/j.msea.2007.11.079>
 30. Zmich R, Meyer D (2021) Thermal Effects on Surface and Subsurface Modifications in Laser-Combined Deep Rolling. *J Manuf Mater Process* 5(2):55. <https://doi.org/10.3390/jmmp5020055>
 31. Altenberger I, Nalla RK, Noster U, Scholtes B, Ritchie RO (2002) On the fatigue behavior and associated effect of residual stresses in deep-rolled and laser shock peened Ti–6Al–4V alloys at ambient and elevated temperatures
 32. Altenberger I, Nalla RK, Sano Y, Wagner L, Ritchie RO (2012) On the effect of deep-rolling and laser-peening on the stress-controlled low- and high-cycle fatigue behavior of Ti–6Al–4V at elevated temperatures up to 550°C. *Int J Fatigue* 44:292–302. <https://doi.org/10.1016/j.ijfatigue.2012.03.008>
 33. Meyer D (2012) Cryogenic deep rolling – An energy based approach for enhanced cold surface hardening. *CIRP Ann* 61(1):543–546. <https://doi.org/10.1016/j.cirp.2012.03.102>
 34. Deutsche Norm. DIN 743–2: Tragfähigkeitsberechnung von Wellen und Achsen: Teil 2: Formzahlen und Kerbwirkungszahlen. DIN 743–2 2012
 35. Forschungskuratorium Maschinenbau (FKM) 2020. FKM-Richtlinie: Rechnerischer Festigkeitsnachweis für Maschinenbauteile: aus Stahl, Eisenguss- und Aluminiumwerkstoffen. FKM-Richtlinie
 36. Kloos KH, Velten B (1984) Berechnung der Dauerschwingfestigkeit von plasmanitierten bauteilähnlichen Proben unter Berücksichtigung des Härte- und Eigenspannungsverlaufs. *Konstruktion* 1984(36):181–188
 37. Saalfeld S, Oevermann T, Niendorf T, Scholtes B (2019) Consequences of deep rolling on the fatigue behavior of steel SAE 1045 at high loading amplitudes. *Int J Fatigue* 118:192–201. <https://doi.org/10.1016/j.ijfatigue.2018.09.014>
 38. Moore MG, Evans WP (1956) Mathematical Correction for Stress in Removed Layers in X-Ray Diffraction Residual Stress Analysis. 1956 <https://doi.org/10.4271/580035>
 39. Savaria V, Bridier F, Bocher P (2012) Computational quantification and correction of the errors induced by layer removal for sub-surface residual stress measurements. *Int J Mech Sci* 64(1):184–195. <https://doi.org/10.1016/j.ijmecsci.2012.07.003>
 40. Denkena B, Abrão A, Krödel A, Meyer K (2020) Analytic roughness prediction by deep rolling. *Prod Eng Res Devel* 14(3):345–354. <https://doi.org/10.1007/s11740-020-00961-0>
 41. Magalhães FC, Abrão AM, Denkena B, Breidenstein B, Mörke T (2017) Analytical Modeling of Surface Roughness, Hardness and Residual Stress Induced by Deep Rolling. *J Mater Eng Perform* 26(2):876–884. <https://doi.org/10.1007/s11665-016-2486-5>
 42. Regazzi D, Cantini S, Cervello S, Foletti S (2017) Optimization of the cold-rolling process to enhance service life of railway axles. *Procedia Structural Integrity* 7:399–406. <https://doi.org/10.1016/j.prostr.2017.11.105>
 43. Hassani-Gangaraj SM, Moridi A, Guagliano M, Ghidini A (2014) Nitriding duration reduction without sacrificing mechanical characteristics and fatigue behavior: The beneficial effect of surface nano-crystallization by prior severe shot peening. *Mater Des* 55:492–498. <https://doi.org/10.1016/j.matdes.2013.10.015>
 44. Lim A, Castagne S, Wong CC (2016) Effect of Deep Cold Rolling on Residual Stress Distributions Between the Treated and Untreated Regions on Ti–6Al–4V Alloy. *J Manuf Sci Eng* 138:11. <https://doi.org/10.1115/1.4033524>
 45. Majzoobi GH, Zare Jouneghani F, Khademi E (2016) Experimental and numerical studies on the effect of deep rolling on bending fretting fatigue resistance of Al7075. *Int J Adv Manuf Technol* 82(9–12):2137–2148. <https://doi.org/10.1007/s00170-015-7542-z>
 46. Manouchehrifar A, Alasvand K (2012) Finite element simulation of deep rolling and evaluate the influence of parameters on residual stress
 47. Bäcker V, Klocke F, Wegner H, Timmer A, Grzhibovskis R, Rjasanow S (2010) Analysis of the deep rolling process on turbine blades using the FEM/BEM-coupling. *IOP Conf Series: Mater Sci Eng* 10:12134. <https://doi.org/10.1088/1757-899X/10/1/012134>
 48. Trauth D, Klocke F, Mattfeld P, Klink A (2013) Time-efficient Prediction of the Surface Layer State after Deep Rolling using Similarity Mechanics Approach. *Procedia CIRP* 9:29–34. <https://doi.org/10.1016/j.procir.2013.06.163>
 49. Sartkulvanich P, Altan T, Jasso F, Rodriguez C (2007) Finite Element Modeling of Hard Roller Burnishing: An Analysis on the Effects of Process Parameters Upon Surface Finish and Residual Stresses. *J Manuf Sci Eng* 129(4):705–716. <https://doi.org/10.1115/1.2738121>
 50. Sayahi M, Sghaier S, Belhadjsalah H (2013) Finite element analysis of ball burnishing process: comparisons between numerical

- results and experiments. *Int J Adv Manuf Technol* 67(5–8):1665–1673. <https://doi.org/10.1007/s00170-012-4599-9>
51. Chaboche JL (1986) Time-independent constitutive theories for cyclic plasticity. *Int J Plast* 2(2):149–188. [https://doi.org/10.1016/0749-6419\(86\)90010-0](https://doi.org/10.1016/0749-6419(86)90010-0)
 52. Chaboche JL (1989) Constitutive equations for cyclic plasticity and cyclic viscoplasticity. *Int J Plast* 5(3):247–302. [https://doi.org/10.1016/0749-6419\(89\)90015-6](https://doi.org/10.1016/0749-6419(89)90015-6)
 53. Chaboche JL (2008) A review of some plasticity and viscoplasticity constitutive theories. *Int J Plast* 24(10):1642–1693. <https://doi.org/10.1016/j.jiplas.2008.03.009>
 54. Ecoroll AG. www.ecoroll.de
 55. European Standard. EN 13261: Railway applications - Wheelsets and bogies - Axles - Product requirements. EN 13261 2021
 56. Linhart V, Černý I (2011) An effect of strength of railway axle steels on fatigue resistance under press fit. *Eng Fract Mech* 78(5):731–741. <https://doi.org/10.1016/j.engfracmech.2010.11.023>
 57. Novosad M, Fajkoš R, Řeha B, Rezníček R (2010) Fatigue tests of railway axles. *Procedia Engineering* 2(1):2259–2268. <https://doi.org/10.1016/j.proeng.2010.03.242>
 58. Thöni C (2014) Auslegung und Planung eines Prüfstandes zur Erzeugung einer umlaufenden Biegespannung an Radsatzwellen. Diplomarbeit. Technische Universität Graz, Graz
 59. European Standard. EN ISO 683–2: Heat-treatable steels, alloy steels and free-cutting steels: Part 2: Alloy steels for quenching and tempering. EN ISO 683–2 2018
 60. European Standard. EN ISO 6892–1 Metallic materials - Tensile testing: Part 1: Method of test at room temperature. EN ISO 6892–1 2022.
 61. International standard. ISO 12106 Metallic materials - Fatigue testing - Axial-strain-controlled method. ISO 12106 2017
 62. Branco R, Costa JD, Antunes FV (2012) Low-cycle fatigue behaviour of 34CrNiMo6 high strength steel. *Theoret Appl Fract Mech* 58(1):28–34. <https://doi.org/10.1016/j.tafmec.2012.02.004>
 63. Branco R, Costa J, Antunes F, Perdigão S (2016) Monotonic and Cyclic Behavior of DIN 34CrNiMo6 Tempered Alloy Steel. *Metals* 6(5):98. <https://doi.org/10.3390/met6050098>
 64. Jahed H (2022) Cyclic Plasticity of Metals: Modeling Fundamentals and Applications. Elsevier, San Diego
 65. European Standard. EN ISO 6506: Metallic materials - Brinell hardness test. EN ISO 6506 2015
 66. European Standard. EN ISO 6507: Metallic materials - Vickers hardness test. EN ISO 6507 2018
 67. ASTM International. ASTM E837 - 13a: Standard Test Method for Determining Residual Stresses by the Hole-Drilling Strain-Gage Method. ASTM E837 - 13a
 68. Sint Technology. Hole drilling method. URL <https://sint-technology.com/>
 69. Gibmeier J, Kornmeier M, Scholtes B (2000) Plastic Deformation during Application of the Hole-Drilling Method. *Mater Sci Forum* 347–349:131–137. <https://doi.org/10.4028/www.scientific.net/MSF.347-349.131>
 70. Lin YC, Chou CP (1995) Error induced by local yielding around hole in hole drilling method for measuring residual stress of materials. *Mater Sci Technol* 11(6):600–604. <https://doi.org/10.1179/mst.1995.11.6.600>
 71. Návrát T, Halabuk D, Vosynek P (2020) Efficiency of Plasticity Correction in the Hole-Drilling Residual Stress Measurement. *Materials* (Basel, Switzerland) 13(15). <https://doi.org/10.3390/ma13153396>
 72. Rossi M, Sasso M, Connesson N, Singh R DeWald A, Backman D, Gloeckner P (2014) Eds. *Residual Stress, Thermomechanics & Infrared Imaging, Hybrid Techniques and Inverse Problems*, Volume 8: Proceedings of the 2013 Annual Conference on Experimental and Applied Mechanics. Springer International Publishing, Cham
 73. Steinzig M, Upshaw D, Rasty J (2014) Influence of Drilling Parameters on the Accuracy of Hole-drilling Residual Stress Measurements. *Exp Mech* 54(9):1537–1543. <https://doi.org/10.1007/s11340-014-9923-x>
 74. Prevey PS (1986) X-Ray Diffraction Residual Stress Techniques. *Metals Handbook* 10(1986):440–458. <https://doi.org/10.31399/asm.hb.v10.a0006632>
 75. Rossini NS, Dassisti M, Benyounis KY, Olabi AG (2012) Methods of measuring residual stresses in components. *Mater Des* 35:572–588. <https://doi.org/10.1016/j.matdes.2011.08.022>
 76. European Standard. EN 15305: Non-destructive testing - Test method for residual stress analysis by X-ray diffraction. EN 15305 2009
 77. Fitzpatrick ME, Fry AT, Holdway P, Kandil F (2002) Determination of residual stresses by X-ray diffraction
 78. Farrahi GH, Lebrun JL (1995) Surface hardness measurement and micro structural characterisation of steel by X-Ray diffraction profile analysis
 79. FernándezPariente I, Guagliano M (2008) About the role of residual stresses and surface work hardening on fatigue ΔK_{th} of a nitrided and shot peened low-alloy steel. *Surf Coat Technol* 202(13):3072–3080. <https://doi.org/10.1016/j.surfcoat.2007.11.015>
 80. Majzoobi GH, Teimoorial Motlagh S, Amiri A (2010) Numerical simulation of residual stress induced by roll-peening. *Trans Indian Inst Met* 63(2–3):499–504. <https://doi.org/10.1007/s12666-010-0071-4>
 81. Han K, Zhang D, Yao C, Tan L, Zhou Z, Zhao Yu (2021) Investigation of residual stress distribution induced during deep rolling of Ti-6Al-4V alloy. *Proc Inst Mech Eng Part B: J Eng Manuf* 235(1–2):186–197. <https://doi.org/10.1177/0954405420947960>
 82. Heikebrügge S, Breidenstein B, Bergmann B, Dänekas C, Schumann P (2022) Experimental and Numerical Investigations of the Deep Rolling Process to Analyze the Local Deformation Behavior of Welded Joints. *J Manuf Mater Process* 6(3):50. <https://doi.org/10.3390/jmmp6030050>
 83. Lyubanova N, Baehre D (2015) Finite Element Modelling and Investigation of the Process Parameters in Deep Rolling of AISI 4140 Steel. *J Mater Sci Eng B* 5(80). <https://doi.org/10.17265/2161-6221/2015.7-8.004>
 84. Lim A, Castagne S, Wong, CC (2014) Effect of friction coefficient on finite element modeling of the deep cold rolling process
 85. MSC Software. Marc Volume A: Theory and User Information - 2020 FP1
 86. Seisenbacher B, Winter G, Grün F (2018) Improved Approach to Determine the Material Parameters for a Combined Hardening Model. *Mater Sci Appl* 09(04):357–367. <https://doi.org/10.4236/msa.2018.94024>
 87. Surtee I, Nobre JP (2016) Residual Stress Redistribution due to Removal of Material Layers by Electrolytic Polishing. *Residual Stresses* 593–598. <https://doi.org/10.21741/9781945291173-100>
 88. Ceglias, RB, Alves, JM, Botelho, RA, Baetajúnior de Souza E, Santos, Igor Cuzzuol dos, M, Nicki Robbers Darciano Cajueiro de O, Rebeca Vieira de D, Saulo Brinco B, Luiz P (2016) Residual Stress Evaluation by X-Ray Diffraction and Hole-Drilling in an API 5L X70 Steel Pipe Bent by Hot Induction. *Mater Res* 19(5):1176–1179. <https://doi.org/10.1590/1980-5373-MR-2016-0012>
 89. Kandil FA, Lord JD, Fry AT, Grant PV (2001) A review of residual stress measurement methods - a guide to technique selection
 90. Rickert T, Fix R, Suominen L (2007) Comparison of Residual Stress Measurements Using X-Ray Diffraction and PRISM - Electronic Speckle Pattern Interferometry and Hole-Drilling. SAE Technical Paper Series. <https://doi.org/10.4271/2007-01-0804>

Publisher's note Springer Nature remains neutral with regard to jurisdictional claims in published maps and institutional affiliations.